



Interplay between timescales governs the residual activity of a harmonically bound active Brownian particle

Sanatan Halder^{1,*} , and Manas Khan^{1,†} 

¹Department of Physics, Indian Institute of Technology Kanpur, Kanpur - 208016, India

Email: *sanatanh@iitk.ac.in, †mkhan@iitk.ac.in

Active microparticles in confining potentials manifest complex and intriguing dynamical phenomena, as their activity competes with confinement. The steady-state position distributions of harmonically bound active Brownian particles (HBABPs) exhibit a crossover from Boltzmann-like to bimodal, commonly recognized as “passive” to “active” transition, upon variation of the activity and the confinement strength. By studying optically trapped phoretically active Janus colloids, along with simulations and analytical calculations of HBABPs, we provide a comprehensive dynamical description emphasizing the resultant velocity to examine this understanding. Our results establish that the crossover is instead from “active” to “passive”-like, and is governed solely by the interplay between the persistence time τ_R , and the equilibration time in harmonic potential τ_k . When $\tau_R < \tau_k$, despite a Boltzmann-like position distribution, the HBABP retains a substantial resultant or residual active velocity, denoting an activity-dominated regime. In contrast, at $\tau_R > \tau_k$, the restoring force fully counterbalances propulsion at a radial distance, where the HBABP exhibits harmonically bound Brownian particle (HBBP)-like dynamics, and the position distribution becomes bimodal. We further provide a quantitative measure of the residual activity, which decreases monotonically with τ_R/τ_k , eventually converging to a nominal value corresponding to HBBP as τ_R/τ_k exceeds 1, corroborating our conclusions.

Introduction – The active dynamics of natural microswimmers, such as bacteria, protozoa, and spermatozoa, and their synthetic counterparts, *e.g.*, self-propelled microparticles, have been major frontiers of contemporary research because of their relevance in describing fundamental nonequilibrium processes and potential applications [1–6]. The most common and perhaps the simplest realization of active microparticles is phoretically propelled half-metal-coated Janus microspheres [7–9]. They are conveniently described as *active Brownian particles* (ABPs), where the active dynamics is modeled by constant propulsion along a direction that is intrinsic to the particle, and hence changes according to their orientational diffusion [2, 5, 6, 10]. Thus, directional persistence fades over a characteristic timescale called the persistence time.

An isolated ABP manifests effective passive-like behaviors at long times as the propulsion direction becomes random unless it interacts with an external potential [10, 11]. However, a confining harmonic potential, which also approximately represents other potentials near a stable point, engenders intriguing nonequilibrium features in ABP dynamics, even in the steady-state, by introducing an additional timescale, *i.e.*, the equilibration time [10–13]. Besides exhibiting a plethora of intricate dynamical phenomena, *e.g.*, accumulation toward the periphery [14–16], self-induced polar ordering [17–19], and anomalous sedimentation [20, 21], confined active dynamics are of importance because they represent the interaction of natural and synthetic active matter with their environment, such as narrow confinements, crowded, porous, and viscoelastic media [5, 22–27]. *Harmonically bound ABPs* (HBABPs) provide an excellent means of modeling and understanding these phenomena and systems.

In recent years, there has been a surge of studies on

HBABPs, mostly employing theoretical approximations [12, 13, 28–33] and numerical simulations [28, 30–32], along with a few experiments [32, 34, 35] exploring a crossover in the steady-state position distribution, which changes from Boltzmann-like to bimodal with increasing strength of harmonic confinement against activity. Complying with the shape of the distributions, this crossover has been commonly identified as equilibrium to strongly nonequilibrium or passive to active transition. However, it remains questionable whether the steady-state position distribution can provide a reliable signature of activity in dynamics. The ABPs also exhibit Boltzmann-like position distributions in the leading order at times much longer than the persistence time [5, 6, 10, 13]. Moreover, it appears inconsistent that an inherently nonequilibrium system shows equilibrium-like behavior under weak confinement, while revealing its nonequilibrium properties when the restoring force field becomes stronger. Therefore, a detailed dynamical analysis is essential to reliably recognize and measure the signature of activity in HBABP dynamics and, consequently, to review the apparent passive-to-active crossover with a complete dynamical description. Although a few studies have investigated and exploited the orbital dynamics of HBABP or analogous inertial systems [36–40], the contribution of activity to the resultant motion has not been explored.

In an experimental study of a phoretically active microsphere in an optical trap complemented by numerical simulations and analytical calculations on an HBABP, we analyze its dynamics, emphasizing the resultant or residual velocity (v_{res}), which reveals the remnant propulsion speed, *i.e.*, its residual activity, at various settings. Our results show that residual activity is governed solely by the interplay between the characteristic timescales, persistence time (τ_R), and equilibration time in the harmonic potential (τ_k).

Intriguingly, a Boltzmann-like to bimodal crossover in the position distributions is accompanied by an exactly opposite transition in the v_{res} distributions, *i.e.*, from bimodal to Gaussian, as τ_R becomes longer than τ_k . Moreover, the residual activity, quantitatively measured by the *root mean square* (rms) value of v_{res} , exhibits a congruent crossover as τ_R/τ_k crosses 1. $(v_{\text{res}})_{\text{rms}}$ decreases monotonically, from being approximately equal to the free propulsion speed at $\tau_R/\tau_k \ll 1$ to that of the corresponding passive case, describing a *harmonically bound Brownian particle* (HBBP) at $\tau_R > \tau_k$. In the latter case, a long-persistent radially outward active motion is completely balanced by the restoring force at a radial distance, where the resultant HBABP dynamics is reduced to that of an HBBP. It performs free azimuthal motion at $t \gg \tau_R$, leading to a bimodal position distribution when projected onto a single dimension.

Thus, we demonstrate that activity-dominated HBABP dynamics with Gaussian steady-state position distributions become effective HBBP dynamics at a finite radial distance without any residual activity as τ_R becomes longer than τ_k . We also show that the propulsion speed, and consequently the Péclet number, does not have any effect on this dynamical crossover. Our findings are further corroborated by the corresponding *mean square displacements* (MSDs), effective force constants, and fluctuation-dissipation analyses.

Active Brownian particle in a harmonic well – The dynamics of an ABP is characterized by active propulsion with a constant speed (V) along an intrinsic direction of the particle, in addition to its passive Brownian motion with a translational diffusion coefficient D_T . Hence, the propulsion direction evolves through orientational diffusion with coefficient D_R , and its correlation decays over a characteristic timescale, *i.e.*, persistence time $\tau_R = 1/D_R$. The two-dimensional (2D) MSD is given by [5, 7, 10]:

$$\langle \Delta r^2(\tau) \rangle = (4D_T + 2V^2\tau_R)\tau + 2V^2\tau_R^2(e^{-\tau/\tau_R} - 1), \quad (1)$$

and the relative contribution of activity to the dynamics is defined by the Péclet number, $\text{Pe} = V/\sqrt{D_R D_T}$ [5].

The Langevin equations describing the translational ($x(t)$, $y(t)$) and orientational ($\phi(t)$) dynamics of an ABP in a harmonic well with force constant k (Fig. 1, EDF 1) can be written as [11]:

$$\begin{aligned} \dot{x} &= v_B^x - x/\tau_k + V \cos \phi, & \dot{y} &= v_B^y - y/\tau_k + V \sin \phi, & \text{and} \\ \dot{\phi} &= v_B^\phi \end{aligned} \quad (2)$$

where, v_B^i , $\tau_k = \gamma_T/k$, and γ_T are the Brownian velocities along \hat{i} ($i = x, y, \phi$), equilibration time, and translational Stokes drag coefficient, respectively.

Platinum-half-coated silica (Pt-silica) microspheres experience active propulsion owing to self-diffusiophoresis in an H_2O_2 solution [7] or self-thermophoresis under laser exposure [8] (Fig. 2, EDF 2, Supplementary Video 1, 2). Thus, its propulsion speed (V) can be controlled by varying H_2O_2 concentration (c) and the laser power (P) (Fig. 2(d, f)).

We use an optical trap to construct a harmonic potential (Fig. 3(a), EDF 3(a), Methods). Because the optical properties of the Pt-coated and uncoated sides of a Janus silica

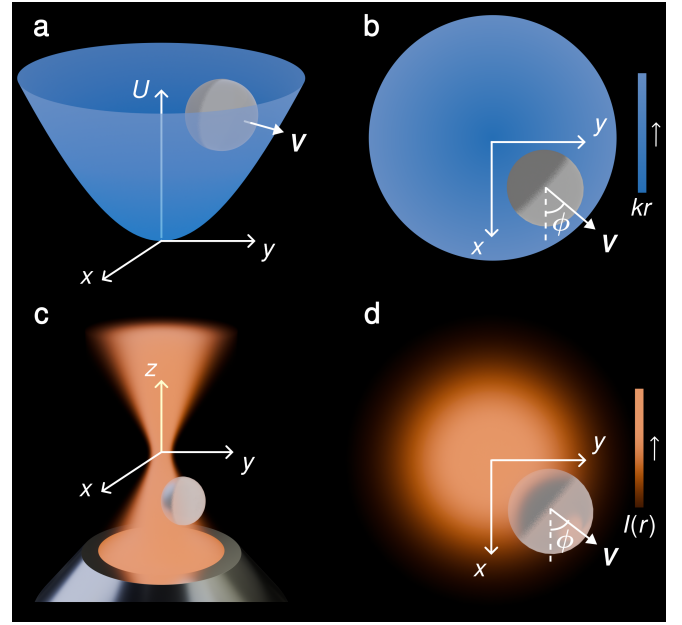


FIG. 1. Schematic (not to scale) of a harmonically bound active Brownian particle (HBABP) and its experimental realization. (a) A Pt-silica Janus colloid (dark grey - light grey sphere) exhibits active Brownian dynamics with a constant propulsion speed V , whose direction evolves with the rotational diffusion of the particle, in a 2D quadratic potential, $U = (1/2)k(x^2 + y^2) = (1/2)kr^2$ (blue). (b) Radial variation in the corresponding restoring force field, $-kr$, is shown as a blue gradient in the $x - y$ plane, where the propulsion direction makes an instantaneous angle $\phi(t)$ with the x -axis. (c) Harmonic confinement of the microsphere is experimentally realized by an optical trap, where a laser beam with a Gaussian intensity profile (orange) is tightly focused by a high-numerical-aperture objective (metallic grey) (EDF 3). The Janus colloid experiences a quadratic potential (Fig. 3(a-b)) and thermophoretic propulsion (Fig. 2(e-h)) as it interacts with the light field. (d) The Gaussian intensity profile (orange gradient) at the focal ($x - y$) plane is shown along with the Janus colloid whose Pt-coated side (dark grey) faces inward, while propulsion (V), which is directed from the Pt-coated side to the bare side, acts radially outward. The propulsion speed (V) is further enhanced by diffusiophoresis (Fig. 2(b-d)) in the presence of H_2O_2 (not shown). The color bars on the right indicate the relative strengths of the respective color gradients.

colloid are different, the forces experienced by the particle vary with its instantaneous orientation and orientation (Fig 3(a), EDF 3(b)). However, the Gaussian and quadratic forms of the long-time ($t \gg \tau_R$, τ_k) position distributions and the corresponding effective potentials at $\tau_R/\tau_k \ll 1$ follow Eq. 3 and Eq. 5, respectively (Fig. 3(b), EDF 7), verifying that the time-averaged confinement experienced by the Janus microsphere is indeed harmonic (Methods). The realized values of τ_R , τ_k , and V are obtained by fitting the MSDs using Eq. 8 (Fig. 3(c), Methods).

We further simulate the HBABP dynamics by numerically solving Langevin equations (Eq. 2), where τ_R , τ_k , and V are varied systematically over a wide range (Methods).

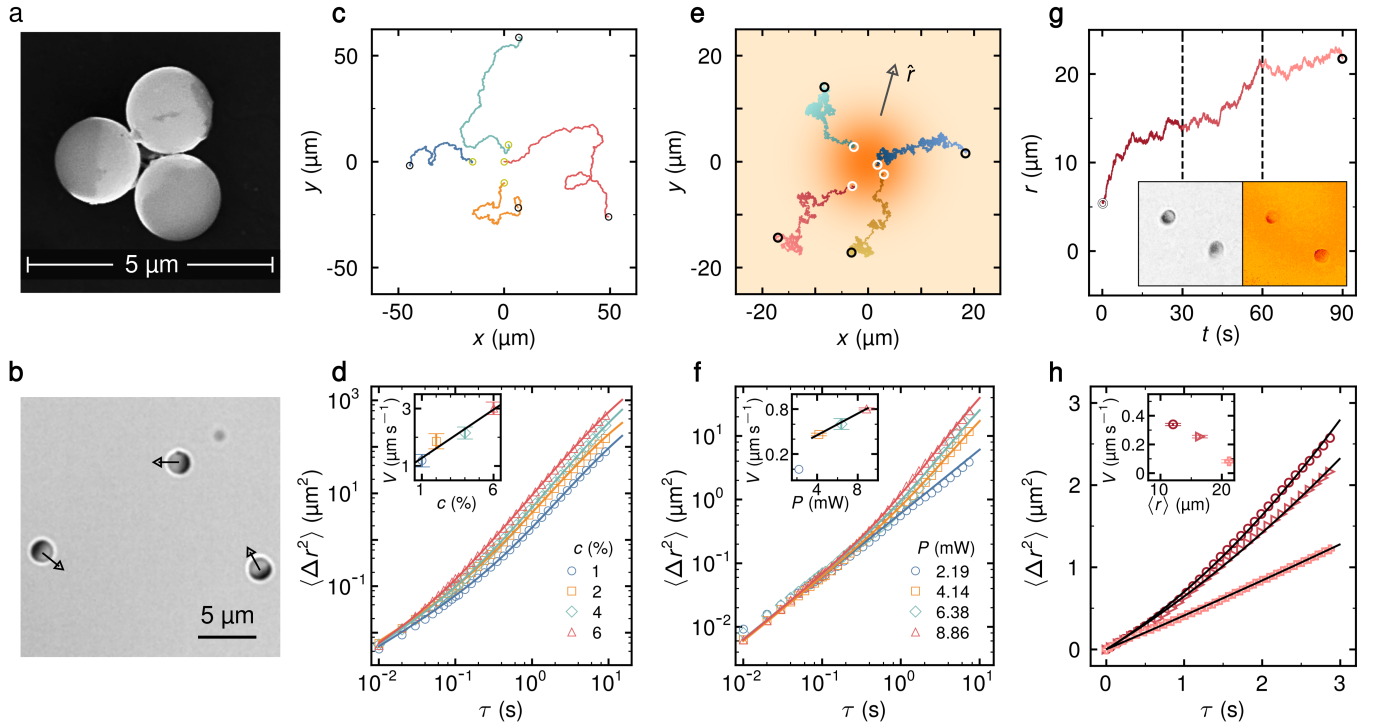


FIG. 2. Experimental realization of active Brownian dynamics. (a) FESEM image shows Janus silica particles (diameter $1.76\ \mu\text{m}$) with Pt coating on one hemisphere, which looks brighter. (b) Self-diffusiophoretic active motions of these Janus colloids in H_2O_2 suspension (EDF 2(b)) are exhibited in a bright-field micrograph, where the coated hemisphere appears darker. The arrows represent the direction of propulsion. (c) Typical trajectories for 45 s and (d) corresponding MSDs (color-coded symbols) of averaged dynamics with increasing H_2O_2 concentration (c) are shown in blue, orange, cyan, and red, respectively. A proportional increase in propulsion speed (V) is obtained by fitting the MSDs to Eq. 1 (solid lines), and is displayed in the inset with a linear fit (black line). (e) Self-thermophoretic active motion of Pt-silica Janus particles under defocused laser illumination (EDF 2(c)) is demonstrated with typical trajectories for 100 s, and (f) the corresponding MSDs (color-coded symbols) at increasing laser power (P) in blue, orange, cyan, and red. The inset shows the variation in time-averaged propulsion speed (V), which is obtained by fitting the MSDs to Eq. 1 (solid lines), and exhibits a linear dependence (black line) on P after a threshold. (g) Background color gradient represents a radially decreasing Gaussian laser intensity profile. Thermophoretic propulsion typically acts along the \hat{r} , while the hotter Pt-coated side faces radially inward. (h) The radial dependence of the instantaneous propulsion speed is shown by plotting $r(t)$ and comparing the radial distances traversed in successive 30 s intervals. (i) This is further demonstrated by plotting the MSDs (color-coded symbols) from these trajectory segments for succeeding 30 s durations. A decreasing variation in V , provided by fitting of the MSDs (black lines), with the mean radial distance $\langle r \rangle$, is shown in the inset. (g inset) Brightfield (left) and corresponding fluorescence (right) micrographs show two immobilized Janus colloids under defocused laser illumination. The fluorescence emission of rhodamine B (orange) from the Pt-coated hemispheres is lower, indicating a higher local temperature (Methods, EDF 2(d)). The error bars for V (insets) denote fitting uncertainties. Standard errors in MSDs are insignificant and hence are not shown.

Trajectory and position distribution – Closed-form solutions for position distributions exist for two limiting cases, $D_R \rightarrow \infty$ and $D_R = 0$ [13, 30]. However, to address practically relevant cases with finite $\tau_R = 1/D_R$, we focus on two quintessential regimes: $\tau_R \ll \tau_k$ and $\tau_R \gg \tau_k$, in which the position distributions exhibit characteristically different features.

When $\tau_R \ll \tau_k$, the propulsion direction becomes random long before the system equilibrates. Thus, $P(x)$ and $P(y)$ evolve into identical zero-mean Gaussians at $t \gg \tau_k$, irrespective of initial conditions, taking the form (Methods)

$$P(x) = \frac{1}{\sqrt{\frac{2\pi k_B T}{k} \left(1 + \frac{\text{Pe}^2}{2}\right)}} \exp \left[\frac{-x^2}{\frac{2k_B T}{k} \left(1 + \frac{\text{Pe}^2}{2}\right)} \right]. \quad (3)$$

A monotonic increase in variance with Pe (FDF 7) indicates activity-dominated dynamics in this regime.

When $\tau_R \gg \tau_k$, the propulsion direction persists longer, and the ABP continues to follow the initial direction (\hat{x}) until it equilibrates, as the restoring force balances the active motion. Here, the activity alters only $P(x)$, which simplifies to a Gaussian with a non-zero mean at $t \gg \tau_k$ (Methods),

$$P(x) = \frac{1}{\sqrt{\frac{2\pi k_B T}{k}}} \exp \left[\frac{-(x - V\tau_k)^2}{2k_B T/k} \right]. \quad (4)$$

Intriguingly, the variance of $P(x)$, $\sigma^2 = k_B T/k$, is independent of V and equal to that of $P(y)$, which describes the corresponding HBBP. However, the mean shifts linearly with V as $\langle x \rangle = V\tau_k = V\gamma_T/k$, i.e., $\langle x \rangle/\sigma = \text{Pe}\sqrt{\tau_k/\tau_R}$, where

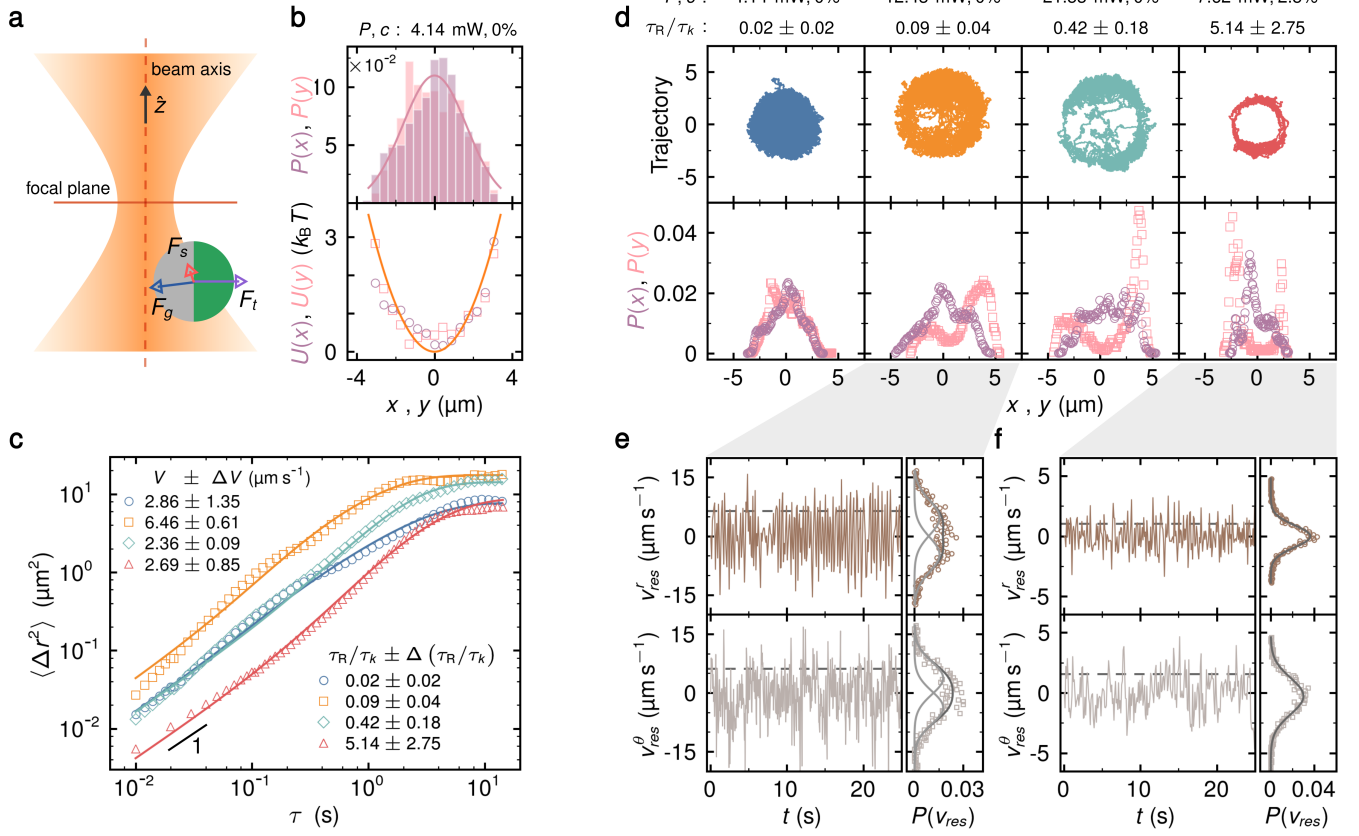


FIG. 3. Experimentally observed dynamics of an optically trapped active Janus colloid. (a) A Pt-silica Janus particle is shown in the intensity field of a tightly focused laser beam propagating along \hat{z} (black arrow), forming an optical trap (Methods, EDF 3). The Janus particle experiences three forces in the laser field: scattering force (F_s), gradient force (F_g), and thermophoretic force (F_t), which vary with the position and orientation of the particle (EDF 3(b)). (b) Long-time position distributions (top, bars) and corresponding effective potentials (bottom, symbols) along both the x - and y -axes are shown using Gaussian and quadratic fits (solid lines), respectively, for a typical case at a lower laser power (4.14 mW). (c) MSDs (symbols) of optically trapped active Janus particles, calculated from the corresponding trajectories (the same color in (d)) at various trap strengths and activities, realized by adjusting the laser power (P) and H_2O_2 concentration (c), are shown for four typical cases. Fitting the MSDs to Eq. 8 (solid lines) provides the values (mean \pm fitting uncertainty) of the respective propulsion speed, V , persistence time (τ_R), and equilibration time (τ_k), and thus their ratio, τ_R/τ_k . (d) Trajectories, recorded at 500 Hz for a 200 s duration, are shown in the order of increasing τ_R/τ_k , from 0.02 to 5.14 (mean), in blue, orange, cyan, and red, respectively. Corresponding position distributions $P(x)$ and $P(y)$ are exhibited in the bottom panel. (e, f) Short segments (25 s) of the time series and probability distributions of the radial and azimuthal components of the residual velocity, v_{res}^r and v_{res}^θ , respectively, calculated from the recorded trajectories averaged over 0.1 s, are shown for the two archetypal regimes: (e) $\tau_R/\tau_k < 1$ and (f) $\tau_R/\tau_k > 1$. The root mean square (rms) values of the velocity components are marked with dashed horizontal lines in the respective time-series plots. While the probability distributions of the residual velocities, $P(v_{\text{res}})$, (e) for $\tau_R/\tau_k < 1$ fit well with the sum of two symmetrically positioned Gaussians (solid lines), those (f) for $\tau_R/\tau_k > 1$ show excellent fitting to a zero-mean Gaussian (solid line).

propulsion is balanced by the restoring force (EDF 7). The propulsion direction changes slowly at $t \gg \tau_R$. Consequently, the position distribution freely moves azimuthally, maintaining $\langle r \rangle = V\gamma_T/k$, and eventually covers an annular region, appearing bimodal in $P(x)$ and $P(y)$.

Comparing the steady-state position distributions (Eq. 3, 4) to that of an HBBP, effective harmonic confinements [28] can be defined by corresponding force constant, k_{eff} , and radial position of the center, r_c :

$$k_{\text{eff}} = \frac{k}{1 + \text{Pe}^2/2}, \quad r_c = 0 \quad \text{for } \tau_R \ll \tau_k, \quad (5)$$

$$k_{\text{eff}} = k, \quad r_c = V\tau_k \quad \text{for } \tau_R \gg \tau_k. \quad (6)$$

Experimentally observed dynamics of an optically trapped Janus particle (Fig 3(d)) validate our analytical predictions. At $\tau_R/\tau_k = 0.02$ and 0.09 ($\ll 1$), the ABP spontaneously crosses the center (Supplementary Video 3) and the spread of the space-filling bound trajectories increases with activity in accordance with Eq. 3. As τ_R/τ_k increases, the trajectories progressively avoid the central region and eventually become annularly confined at $\tau_R/\tau_k = 5.14$ (Supplementary Video 4). Corresponding position distributions, even before reaching steady-state, exhibit signatures of a crossover from zero-mean Gaussian (Eq. 3) to bimodal distribution (Eq. 4) with increasing τ_R/τ_k , irrespective of V . The simulated steady-state dynamics at higher V values

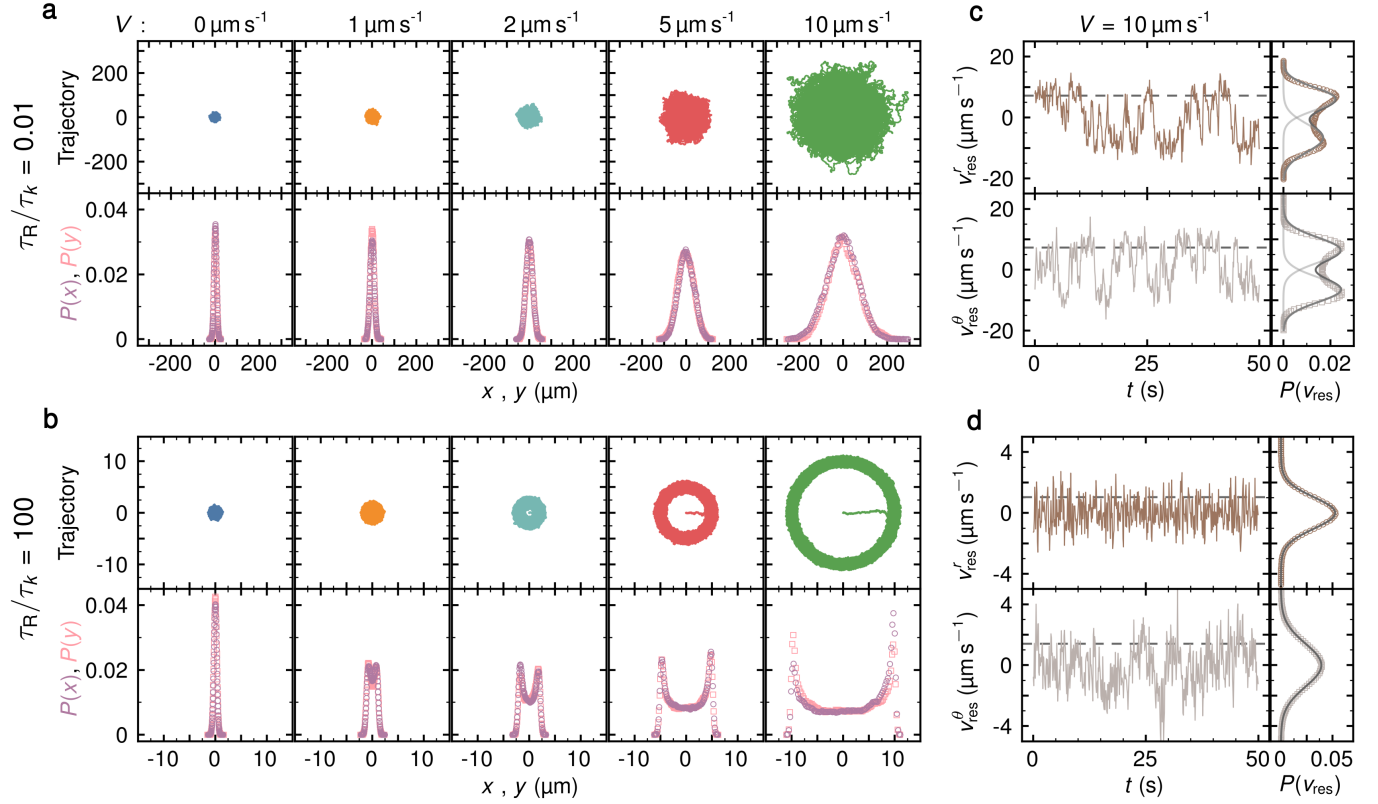


FIG. 4. Numerically simulated dynamics of a harmonically bound active Brownian particle (HBABP). (a, b) Five simulated trajectories of 10^5 s duration, generated at 10^3 Hz, (top panels) with increasing propulsion speed (V), starting from 0, *i.e.*, corresponding to an HBBP, to $10 \mu\text{m/s}$, are shown in blue, orange, cyan, red, and green for two dynamically different regimes at widely varied ratios of the timescales: (a) $\tau_R/\tau_k = 0.01$ with $\tau_R = 1$ s, and $\tau_k = 100$ s; and (b) $\tau_R/\tau_k = 100$ with $\tau_R = 100$ s, and $\tau_k = 1$ s. The bottom panels exhibit the corresponding steady-state position distributions $P(x)$ and $P(y)$ with color-coded circles and squares, respectively. (c, d) Short segments (50 s) of the time series and probability distributions of the radial and tangential components of the residual velocities, v_{res}^r and v_{res}^θ , respectively, calculated from the trajectories with $V = 10 \mu\text{m/s}$, averaged over 0.1 s, are shown for the two quintessential cases: (c) $\tau_R/\tau_k (= 0.01) < 1$, and (d) $\tau_R/\tau_k (= 100) > 1$. The horizontal dashed lines in the time series plots represent the respective rms values. The probability distributions of the residual velocities, $P(v_{\text{res}})$, (c) for $\tau_R/\tau_k < 1$ show bimodal distributions, which fit well to the sum of the two symmetrically positioned Gaussians (solid lines). Their counterparts (d) for $\tau_R/\tau_k > 1$ fit perfectly to single zero-mean Gaussians (solid lines).

make the pertinent features more apparent (Fig 4 (a, b)), corroborating our analytical results. For $\tau_R/\tau_k = 0.01$, the direction of propulsion changes faster, and the isotropic dynamics of the ABP frequently crosses the central region to cover a bound area (Supplementary Video 5). The variance of the corresponding Gaussian position distributions increases with V , validating Eq. 3 (EDF 7). When $\tau_R/\tau_k = 100$, the direction of active motion persists longer, and the ABP propels radially outward until the restoring force equalizes the propulsion. The slow reorientation of the particle causes azimuthal dynamics (Supplementary Video 6), leading to annularly confined trajectories at long time. The peaks of the corresponding bimodal position distributions shift outwards with increasing V , following Eq. 4 (EDF 7).

Residual velocity – We define the residual velocity, v_{res} , of the HBABP as the resultant velocity (Eq. 2), which provides signatures of excess propulsion after countering harmonic confinement. Exploiting circular symmetry, we analyze its

radial (v_{res}^r) and azimuthal (v_{res}^θ) components as:

$$v_{\text{res}}^r = V^r - r/\tau_k + v_B^r \quad \text{and} \quad v_{\text{res}}^\theta = V^\theta + v_B^\theta. \quad (7)$$

When $\tau_R/\tau_k \ll 1$ (Fig. 3(e) and 4(c)), the probability distributions for both velocity components are flat-topped Gaussians (Fig. 3(e)) or bimodal (Fig. 4(c)), consisting of two Gaussians symmetrically placed at approximately the corresponding rms value. Moreover, $\langle (v_{\text{res}}^r)^2 \rangle + \langle (v_{\text{res}}^\theta)^2 \rangle \approx V^2$ indicates that the ABP retains nearly the same propulsion speed even under harmonic confinement. Because the propulsion direction changes rapidly, there is rarely a balance between fast-varying V^r and r/τ_k (Supplementary Video 5).

For $\tau_R/\tau_k \gg 1$ (Fig. 3(f) and 4(d)), both v_{res}^r and v_{res}^θ have zero-mean Gaussian probability distributions with significantly smaller rms values, resembling HBBP dynamics. A slowly changing propulsion direction ensures that V^r is continually counterbalanced by r/τ_k at $r = V\tau_k$. A slowly

developing $V^\theta(\theta)$ leads the ABP to an azimuthal position (θ) where it vanishes and thus remains systematically insignificant (Supplementary Video 6).

Mean square displacement – The 2D MSD, $\langle \Delta r^2 \rangle$ is analytically derived as (Methods),

$$\langle \Delta r^2(\tau) \rangle = \frac{4k_B T}{k} [1 - e^{-\tau/\tau_k}] + \frac{2V^2 \tau_k^2 \tau_R}{\tau_R + \tau_k} \left[1 - \frac{\tau_R e^{-\tau/\tau_R} - \tau_k e^{-\tau/\tau_k}}{\tau_R - \tau_k} \right]. \quad (8)$$

When $\tau_R/\tau_k \ll 1$, it simplifies to,

$$\langle \Delta r^2(\tau) \rangle = \left(\frac{4k_B T}{k} + 2V^2 \tau_k \tau_R \right) [1 - e^{-\tau/\tau_k}] + 2V^2 \tau_R^2 e^{-\tau/\tau_R}. \quad (9)$$

The MSD at intermediate time-lags is dominated by the last term, which varies as $V^2 \tau^2$ at $\tau < \tau_R$, thus verifying the presence of active dynamics. After a linear increase in $\tau_R < \tau < \tau_k$, it eventually saturates at $\tau > \tau_k$.

With $\tau_R/\tau_k \gg 1$, Eq. 8 takes the form

$$\langle \Delta r^2(\tau) \rangle = \frac{4k_B T}{k} [1 - e^{-\tau/\tau_k}] + 2V^2 \tau_k^2 [1 - e^{-\tau/\tau_R}]. \quad (10)$$

MSD is the sum of two terms that increase linearly before reaching plateaus at $\tau > \tau_k$ and $\tau > \tau_R$. This indicates the absence of a steady active motion. A set of k_{eff} and r_c can be defined by comparing the steady-state MSD values with that of HBBP (Methods); they are the same as those in Eq. 5 and 6.

The MSDs of active Janus particles in optical trap fit well with Eq. 8 (Fig. 3(c)). Despite having similar V , the MSDs with $\tau_R/\tau_k = 0.02$ and 0.42 (< 1) manifest activity dominated dynamics, being significantly higher than the one with $\tau_R/\tau_k > 5.14$. The presence of activity at $\tau_R/\tau_k = 0.02$ and 0.09 ($\ll 1$) is further corroborated by a 4 to 6 times increase in MSD as V becomes ~ 2.5 times.

The MSDs from the simulated dynamics exhibit excellent agreement with Eq. 8 (Fig 5). At $\tau_R/\tau_k = 0.01$ (Fig 5(a)), a clear emergence of τ^2 dependence as τ approaches τ_R validates activity-dominated dynamics. For $\tau_R/\tau_k = 100$ (Fig 5(b)), the MSDs mostly increase linearly before saturation and remain 10 - 100 times smaller than their counterparts in the former case, despite having 20 times higher Pe. While the MSDs for smaller V values show two clear plateaus, the one at longer τ suppresses the first plateau for larger V .

Residual activity – We provide a quantitative measure of the residual activity with $(v_{\text{res}})_{\text{rms}}$, *i.e.*, the rms value of the residual or resultant velocity (Eq. 7). It decreases with increasing values of τ_R/τ_k , with a crossover at $\tau_R/\tau_k = 1$, irrespective of V and Pe (Fig. 6(a)). When $\tau_R/\tau_k \ll 1$, $(v_{\text{res}})_{\text{rms}}$ exceeds V with an additional contribution from v_{HBBP} . Maintaining a decreasing trend, v_{res} retains part of the propulsion speed at $\tau_R/\tau_k = 1$. With $\tau_R/\tau_k > 1$, all $(v_{\text{res}})_{\text{rms}}$ values converge to the corresponding $(v_{\text{HBBP}})_{\text{rms}}$, verifying the absence of any residual activity. In this regime, propulsion is fully balanced by the restoring force at $r = V^r \tau_k$.

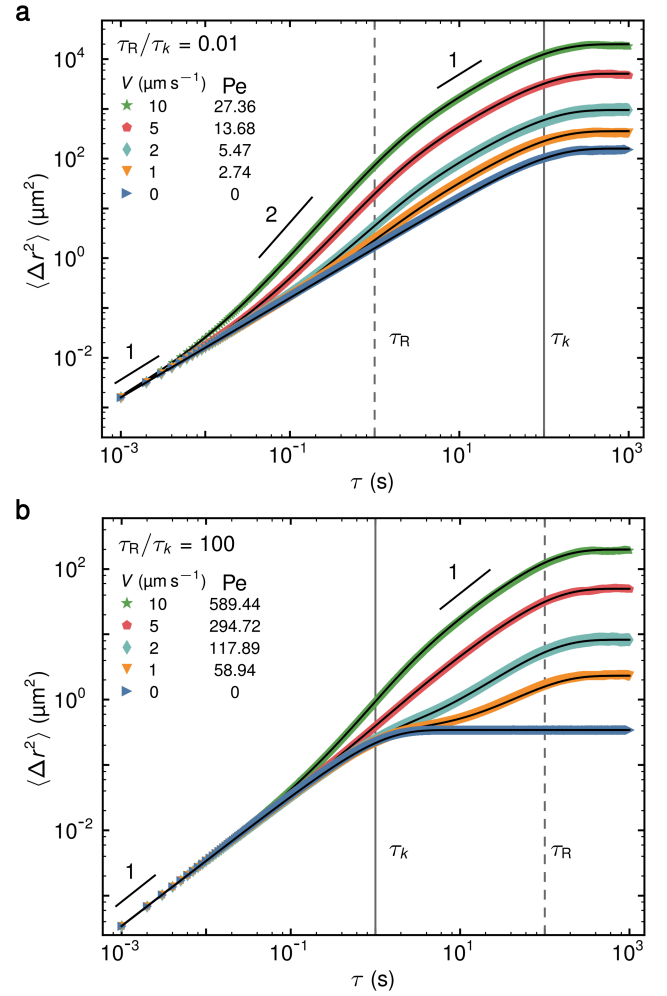


FIG. 5. MSDs from simulated trajectories of a harmonically confined active Brownian particle. Computed MSDs with five different propulsion speeds (V), starting from 0, which essentially represents an HBBP, to $10 \mu\text{m/s}$, are shown for two characteristic cases: (a) $\tau_R/\tau_k (= 0.01) < 1$ and (b) $\tau_R/\tau_k (= 100) > 1$, with symbols of the same colors as those of the corresponding trajectories exhibited in Fig. 4 (a, b). Five propulsion speeds (V) and the corresponding Peclet numbers (Pe) are specified in the insets. The fittings of the MSDs to the analytical solution (Eq. 8) are shown with solid black lines. The characteristic timescales, persistence time (τ_R), and equilibration time (τ_k) are marked with dashed and solid vertical lines, respectively, and the apparent slopes of 1 and 2 are indicated by short black straight lines of the corresponding slopes as visual guides.

To validate our findings further, we analyze the position distributions and power spectral densities (PSD) of the resultant dynamics along the positive x and y directions (Methods). At $\tau_R/\tau_k \ll 1$, the steady-state position distributions are zero-mean Gaussians that broaden with increasing V (Fig. 6(b)). Consequently, k_{eff} decreases, thus validating Eq. 5 (EDF 7(a-c)). Corresponding PSDs deviate from that dictated by the fluctuation dissipation theorem (FDT) at frequencies where propulsion dominates Brownian dynamics (Fig. 6(c), Methods). When $\tau_R/\tau_k \gg 1$, the radial po-

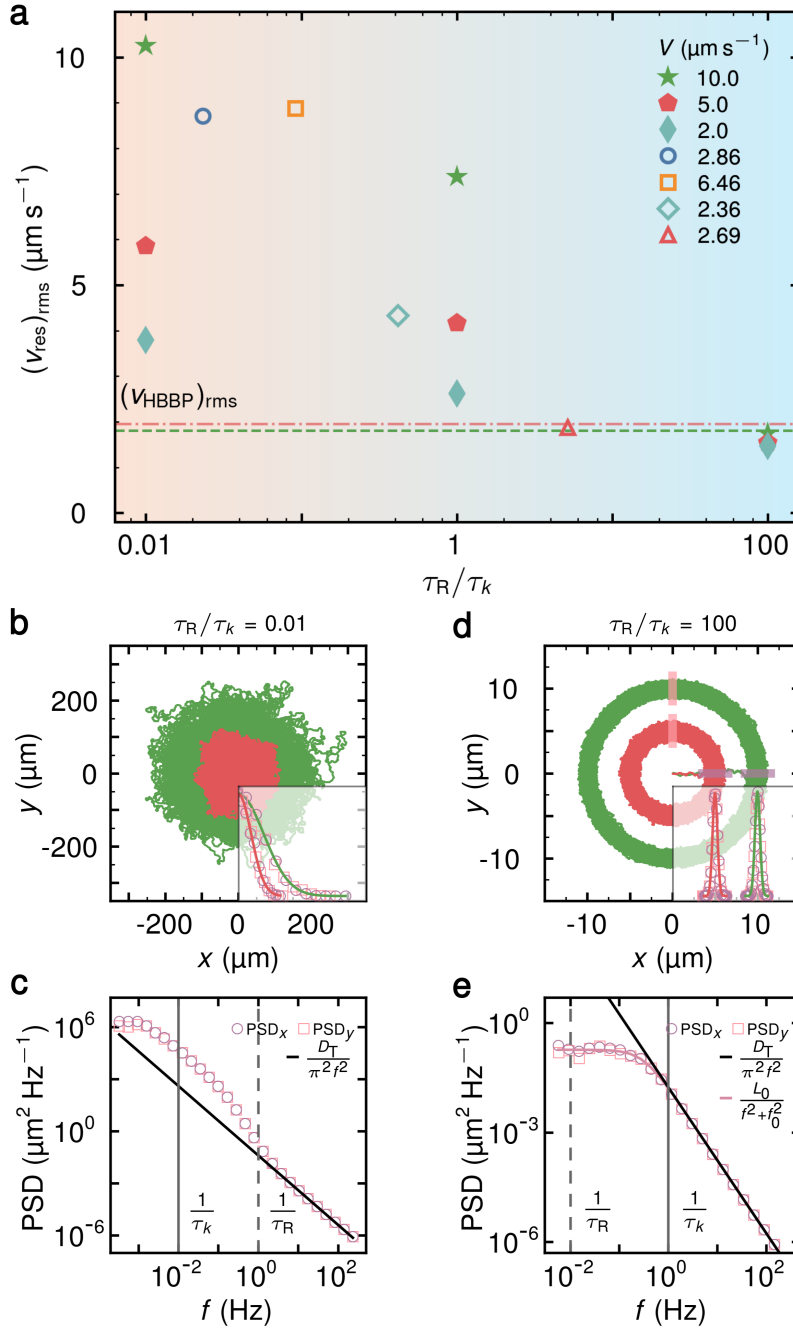


FIG. 6. Variation in residual activity with the ratio of characteristic timescales, τ_R/τ_k . (a) The rms values of the residual propulsion speeds, $(v_{\text{res}})_{\text{rms}}$, for various values of V from all observations, including experiments (open symbols) and simulations (filled symbols), are plotted against the respective values of τ_R/τ_k . The V values corresponding to each symbol are presented in the inset. For cases with $\tau_R/\tau_k > 1$, the theoretical values of $(v_{\text{res}})_{\text{rms}}$ for an HBBP of the same size, *i.e.*, for $V = 0$, $((v_{\text{HBBP}})_{\text{rms}} = \sqrt{(4D_T/\Delta t) - (2D_T/\tau_k)}$, where $\Delta t = 0.1$ s) are indicated by the color-coded dashed horizontal lines for reference. The $(v_{\text{HBBP}})_{\text{rms}}$ values for all three data points at $\tau_R/\tau_k = 100$ with varied V are the same and hence are marked by a single (green) line. The background color gradient implies a crossover in residual activity with τ_R/τ_k . The strength of residual activities in the two archetypal regimes, $\tau_R/\tau_k < 1$ and $\tau_R/\tau_k > 1$, are further demonstrated by the steady-state position distributions and power spectral densities (PSD) for $\tau_R/\tau_k = 0.01$, and $\tau_R/\tau_k = 100$ in the left (b, c) and right (d, e) columns, respectively. (b, d) Steady-state position distributions are shown for positive x (circles) and y (squares) by overlaying them on trajectories with $V = 10 \mu\text{m/s}$ (green) and $5 \mu\text{m/s}$ (red). In (d), the position distributions for x and y are calculated from the trajectory segments in thin rectangular strips (highlighted on the trajectory) on the positive x - and y -axes, respectively. Gaussian fits to the probability distributions are shown using color-coded lines. (c, e) PSDs along x (circles) and y (squares), calculated from (b) the trajectory, or (d) the trajectory segments for $V = 10 \mu\text{m/s}$, are compared with the FDT prediction for the PSD of a free Brownian particle ($D_T/\pi^2 f^2$), shown as black straight lines. The PSDs in (e) fits perfectly with a Lorentzian, given by $L_0/(f^2 + f_0^2)$ (violet line), which represents the PSD of an HBBP. The solid and dashed vertical lines indicate the frequencies corresponding to the characteristic timescales τ_k and τ_R , respectively.

sition distributions are Gaussians with nonzero mean that increases linearly with V , whereas the variance, and thus k_{eff} , remains unchanged, corroborating Eq. 6 (Fig. 6(d), EDF 7(d-f)). Moreover, the PSDs validate the FDT beyond corner-frequency and fit perfectly to Lorentzian, confirming HBBP-like dynamics (Fig. 6(e), Methods).

These results unequivocally conclude that, as τ_R/τ_k crosses 1, the residual-activity-dominated confined dynamics transform into radially displaced HBBP-like dynamics without any residual activity.

Discussion – By analyzing the resultant dynamics of an HBABP and its experimental realization, *i.e.*, an optically trapped phoretically active microsphere, we demonstrate that the resultant velocity (v_{res}), and thereby its residual activity, defined as $(v_{\text{res}})_{\text{rms}}$, is solely governed by the ratio of the characteristic timescales, τ_R/τ_k . When $\tau_R/\tau_k < 1$, although the steady-state position distribution is Boltzmann-like, which is reminiscent of passive dynamics, the presence of higher residual activity is distinctly manifested by bimodal distributions of v_{res} with a higher $(v_{\text{res}})_{\text{rms}}$, larger MSDs, propulsion-speed-dependent k_{eff} , and a clear violation of the FDT. In contrast, at $\tau_R/\tau_k > 1$, the resultant dynamics are essentially reduced to HBBP motions at $r = V\tau_k$, where radially outward propulsion is fully compensated by the restoring force. Here, zero-mean Gaussian distributions of v_{res} , propulsion-speed-independent k_{eff} , and Lorentzian PSD verify the absence of any residual activity despite having a bimodal position distribution. The propulsion speed or Pe does not affect this crossover from activity-dominated to passive-like dynamics. However, they regulate the width and radial shift of the position distributions, and consequently, the strength (k_{eff}) and radial position (r_c) of the effective harmonic confinement in the former and latter cases, respectively (EDF 7).

Existing studies identified the Boltzmann-like and bimodal steady-state position distributions of HBABPs as signature of passive and active regimes, respectively, without exploring its resultant velocity [28–31, 33–35]. With a complete dynamical analysis of the resultant motion, we establish that the randomization of the propulsion direction at $t \gg \tau_R$ causes Boltzmann-like position distributions in a residual-activity-dominated regime, whereas a free azimuthal motion of a radially displaced HBBP, devoid of residual activity, leads to an annularly confined trajectory and bimodal position distribution in one-dimension.

Intriguingly, harmonically bound active Ornstein–Uhlenbeck [41] or run-and-tumble dynamics [20], without a well-defined directional persistence timescale (τ_R), do not exhibit such a dynamical crossover. This further validates our conclusion that this crossover is entirely dictated by the interplay between timescales. Furthermore, Pe no longer remains a measure of activity for HBABPs; a higher Pe at the same V indicates a longer τ_R and, consequently, reduced residual activity at larger τ_R/τ_k .

Although an HBABP trajectory at $\tau_R/\tau_k \gg 1$ eventually covers a full circle with random azimuthal motion, it is fundamentally different from the deterministic circulatory dynamics of a chiral ABP driven by a constant torque [42]. Re-

markably, the effective confinement parameters k_{eff} and r_c provide a complete description of the steady-state HBABP dynamics, unlike the effective temperature, which characterizes only the enhanced transport of ABPs [5, 10, 43].

Our study provides a reliable quantification of the manifestation of activity, and thereby the deviation from equilibrium [44, 45], besides offering a viable approach for describing the mechanical pressure of active systems under confinement [46]. Studying and comparing residual activities in run-and-tumble and chiral ABP motions in harmonic and other anharmonic confinements [20, 47] remain important future directions. Investigating the coupling between spinning and orbital dynamics [39, 48] of optically trapped Janus colloids also presents an interesting extension. Furthermore, confining ABPs to dynamically varying potentials, *e.g.*, time-dependent or slow-moving optical traps [49–52] provides an excellent means to study their interactions with complex environments.

Methods

A | Theoretical description of an HBABP

Positions – $x(t)$ can be derived from Eq. 2 as [11, 53],

$$x(t) = e^{-t/\tau_k} \left[x_0 + \int_0^t e^{t'/\tau_k} \{v_B^x(t') + V \cos(\phi(t'))\} dt' \right],$$

where $x_0 \equiv x(t=0)$. Similarly, $y(t)$, with $y_0 \equiv y(t=0)$, can be obtained as,

$$y(t) = e^{-t/\tau_k} \left[y_0 + \int_0^t e^{t'/\tau_k} \{v_B^y(t') + V \sin(\phi(t'))\} dt' \right].$$

By expressing the translational velocity terms consisting of the passive (v_B^x) and active ($V \cos \phi(t)$) contributions as $\{v_B^x(t) + V \cos(\phi(t))\} = A^x(t)$, their first and second moments are given by (Supplementary Notes),

$$\langle A^x(t) \rangle = V \cos(\phi_0) e^{-t/\tau_R}, \quad (\text{A1})$$

$$\langle A^y(t) \rangle = V \sin(\phi_0) e^{-t/\tau_R}, \quad (\text{A2})$$

$$\langle A^x(t_1) A^x(t_2) \rangle = 2D_T \delta(t_1 - t_2) + V^2 \langle \cos \phi(t_1) \cos \phi(t_2) \rangle, \quad (\text{A3})$$

$$\langle A^y(t_1) A^y(t_2) \rangle = 2D_T \delta(t_1 - t_2) + V^2 \langle \sin \phi(t_1) \sin \phi(t_2) \rangle. \quad (\text{A4})$$

The cross-terms cancel out because the Brownian translational and orientational noises are uncorrelated, and $\phi_0 \equiv \phi(t=0)$.

Position distributions – $P(x)$ and $P(y)$ are derived for two characteristically different regimes, $\tau_R \ll \tau_k$ and $\tau_R \gg \tau_k$, using a lemma [54] that states if $R(t) = \int_0^t \psi(t') A_B(t') dt'$, where $A_B(t)$ is a Gaussian random variable with $\langle A_B(t) \rangle = 0$ and $\langle A_B(t_1) A_B(t_2) \rangle = 2q\delta(t_1 - t_2)$, then

$$P(R) = \frac{1}{[4\pi q \int_0^t \psi^2(t') dt']^{1/2}} \exp \left(-\frac{|R|^2}{4q \int_0^t \psi^2(t') dt'} \right).$$

For $\tau_R \ll \tau_k$, τ_R can be considered insignificantly short for all practical purposes, i.e., $\tau_R \rightarrow 0$. The mean (Eq. A1 and A2) and time-correlation (Eq. A3 and A4) of $A^x(t)$ and $A^y(t)$ become zero and delta-correlated, respectively, at $t \gg \tau_R$. This allows the lemma to be used to obtain $P(x, x_0; t)$ and $P(y, y_0; t)$ (supplementary Notes). They have the same form, which is given by,

$$P(x, x_0; t) = \frac{1}{\sqrt{2\pi\sigma_{1,t}^2}} \exp \left[-\frac{(x - x_0 e^{-t/\tau_k})^2}{2\sigma_{1,t}^2} \right], \quad (\text{A5})$$

where $\sigma_{1,t}^2 = \frac{k_B T}{k} \left(1 + \frac{\text{Pe}^2}{2}\right) (1 - e^{-2t/\tau_k})$.

At steady-state, $t \gg \tau_k \gg \tau_R$, $\sigma_{1,t}^2 \rightarrow \sigma_1^2 = \frac{k_B T}{k} \left(1 + \frac{\text{Pe}^2}{2}\right)$, and Eq. A5 is reduced to Eq. 3. The corresponding 2D position distribution becomes

$$P(r) = \frac{k}{2\pi k_B T \left(1 + \frac{\text{Pe}^2}{2}\right)} \exp \left[-\frac{kr^2}{2k_B T \left(1 + \frac{\text{Pe}^2}{2}\right)} \right]. \quad (\text{A6})$$

When $\tau_R \gg \tau_k$, propulsion continues to follow its initial direction, i.e., \hat{x} , for $t < \tau_R$, until the ABP equilibrates in the harmonic well. At $t < \tau_R$, $\phi(t)$ maintains its initial value of $\phi_0 = 0$. Consequently, $P(y, y_0; t)$ remains unaffected by activity and has the same form as that of a HBBP (Supplementary Notes). With constant propulsion along x , translational noise $A^x(t)$ has only $v_B^x(t)$ and is analogous to $A_B(t)$. Applying the lemma with $R(t) = x - x_0 e^{-t/\tau_k} - V\tau_k(1 - e^{-t/\tau_k})$, we obtain

$$P(x, x_0; t) = \frac{1}{\sqrt{2\pi\sigma_{2,t}^2}} \exp \left[-\frac{((x - V\tau_k) - (x_0 - V\tau_k) e^{-t/\tau_k})^2}{2\sigma_{2,t}^2} \right], \quad (\text{A7})$$

where $\sigma_{2,t}^2 = \frac{k_B T}{k} (1 - e^{-2t/\tau_k})$ is the same as that of the corresponding HBBP (Supplementary Notes).

At $t \gg \tau_k$, with $\sigma_2^2 \equiv \sigma^2 = \frac{k_B T}{k}$, Eq. A7 is reduced to Eq. 4. Over a longer time, as the steady-state is reached at $t \gg \tau_R \gg \tau_k$, slow orientational diffusion of the HBABP leads to free azimuthal motion of the Gaussian position distribution (Eq. 4). Thus, the 2D position distribution becomes (Supplementary Notes)

$$P(r) = \frac{k}{2\pi k_B T} \exp \left[-\frac{(r - V\tau_k)^2}{2k_B T/k} \right], \quad (\text{A8})$$

which appears bimodal with peaks at $\pm V\tau_k$ when projected onto a single axis.

Mean square displacements – The MSDs are defined and calculated as $\langle \Delta r^2(\tau) \rangle = \langle (r(t+\tau) - r(t))^2 \rangle_t$ in the main text. However, for convenience, it is derived here as $\langle \Delta r^2(t) \rangle = \langle (r(t) - r(0))^2 \rangle$.

Therefore, the MSD along \hat{x} is given by $\langle (x(t) - x(0))^2 \rangle = [\langle x^2(t) \rangle + \langle x^2(0) \rangle - 2\langle x(t)x(0) \rangle]$. From the expressions for $x(t)$ and $x(0)$, we obtain (Supplementary Notes),

$$\langle x(t)x(0) \rangle = \frac{k_B T}{k} e^{-t/\tau_k} + \frac{V^2}{2} \frac{\tau_R \tau_k^2 (\tau_R e^{-t/\tau_R} - \tau_k e^{-t/\tau_k})}{(\tau_R + \tau_k)(\tau_R - \tau_k)} + I_1 \cos 2\phi_0,$$

and

$$\langle x^2(t) \rangle = \langle x^2(0) \rangle = \frac{k_B T}{k} + \frac{V^2}{2} \frac{\tau_R \tau_k^2}{(\tau_R + \tau_k)} + I_2 \cos 2\phi_0,$$

where I_1 and I_2 are two exponential integrals. Therefore, $\langle \Delta x^2(t) \rangle$ is given by

$$\langle (x(t) - x(0))^2 \rangle = \frac{2k_B T}{k} (1 - e^{-t/\tau_k}) + \frac{V^2 \tau_R \tau_k^2}{(\tau_R + \tau_k)} \left[1 - \frac{\tau_R e^{-t/\tau_R} - \tau_k e^{-t/\tau_k}}{(\tau_R - \tau_k)} \right] + 2(I_2 - I_1) \cos 2\phi_0.$$

Following similar steps, $\langle \Delta y^2(t) \rangle$ is derived as

$$\langle (y(t) - y(0))^2 \rangle = \frac{2k_B T}{k} (1 - e^{-t/\tau_k}) + \frac{V^2 \tau_k^2 \tau_R}{(\tau_R + \tau_k)} \left[1 - \frac{\tau_R e^{-t/\tau_R} - \tau_k e^{-t/\tau_k}}{(\tau_R - \tau_k)} \right] - 2(I_2 - I_1) \cos 2\phi_0.$$

Finally, Eq. 8 is obtained as $\langle \Delta r^2(t) \rangle = \langle \Delta x^2(t) \rangle + \langle \Delta y^2(t) \rangle$ and agrees with the existing results [8].

The MSD expression in Eq. 8 diverges for the special case $\tau_R = \tau_k = \tau_{eq}$. However, this case can be addressed by considering $\tau_R \rightarrow \tau_k$ limit to derive the MSD

$$\langle \Delta r^2(t) \rangle = \frac{4k_B T}{k} (1 - e^{-t/\tau_{eq}}) + V^2 \tau_{eq}^2 \left[1 - e^{-t/\tau_{eq}} \left(1 - \frac{t}{\tau_{eq}} \right) \right].$$

Effective harmonic confinement description from MSD – Comparing the steady-state expressions for MSD at $\tau_R \ll \tau_k$ and $\tau_R \gg \tau_k$ with that of HBBP, k_{eff} and r_c are obtained.

For $\tau_R \ll \tau_k$, the MSD (Eq. 9) at steady-state ($t \gg \tau_k$) becomes

$$\langle \Delta r^2 \rangle = \frac{4k_B T}{k} + 2V^2 \tau_k \tau_R = \frac{4k_B T}{k} \left(1 + \frac{V^2}{2D_R D_T} \right). \quad (\text{A9})$$

Similarly, at steady-state ($t \gg \tau_R$), the MSD for $\tau_R \gg \tau_k$ (Eq. 10) is given by

$$\langle \Delta r^2 \rangle = \frac{4k_B T}{k} + 2V^2 \tau_k^2. \quad (\text{A10})$$

Comparing Eq. A9 and Eq. A10 with the steady-state MSD of an HBBP, $\langle \Delta r^2 \rangle = 4k_B T/k$, k_{eff} and r_c are defined as,

$$\begin{aligned} k_{eff} &= k / \left(1 + \text{Pe}^2/2 \right), & r_c &= 0 & \text{for } \tau_R \ll \tau_k, \\ k_{eff} &= k, & r_c &= V\tau_k & \text{for } \tau_R \gg \tau_k. \end{aligned}$$

These expressions are the same as those in Eq. 5 and 6 (EDF 7).

B | Active dynamics of Janus colloids in an optical trap

Preparation of Pt-silica Janus colloids – A uniform monolayer of silica microspheres (diameter 1.76 μm , microparticles GmbH) was formed on a plasma-cleaned glass plate by slow evaporation at low temperature ($\sim 4^\circ\text{C}$). A thin (~ 5.5 nm) platinum layer was deposited on the monolayer using a plasma sputter coater, where only the exposed upper hemisphere of the silica microspheres became platinum-coated (Fig. 2(a), EDF 2(a)) [55]. The half-coated microspheres were peeled from the glass plate and washed by repeated resuspension and centrifugation. The final dilute suspension was prepared in deionized water for further use.

Self-diffusiophoretic active motion – When H_2O_2 is added to a suspension of Pt-silica Janus colloids, it dissociates into H_2O and O_2 at the Pt-coated surface, which acts as a catalyst (EDF 2(b)). This process creates a local concentration gradient and consequently induces a local hydrodynamic flow. In response, the Pt-silica Janus particles experience diffusiophoretic propulsion, which changes direction with orientation (Supplementary Video 1) [56]. The active motion of Janus colloids was characterized at various H_2O_2 concentrations, c , measured as the ratio of volumes, from 1% to 6%, where V increased linearly with c (Fig. 2(c-d)) [7].

Self-thermophoretic active motion – Under laser exposure, the Pt-coated side of the Janus colloids becomes hotter by absorbing more than the uncoated side (EDF 2(c)). The absorption coefficient of the Pt thin film is ≈ 0.45 [57], whereas silica is almost transparent at the working wavelength of 1064 nm [58]. This creates a temperature gradient and consequently a convective flow across the Janus colloid. In response, Pt-silica particles experience thermophoretic propulsion along an instantaneous negative temperature gradient owing to their positive Soret coefficient [8]. Thus, in the laser field, Janus colloids moved radially outward, with the hotter Pt-coated side pointing radially inward (Fig. 2(e), Supplementary Video 2). The variations in the instantaneous propulsion speed (V) with the radial distance (r) and laser power (P) are shown in Fig. 2(f-h). Although the thermophoretic active motion of other microspheres has been reported in the literature [8, 39, 59–61], ours is the first such observation for Pt-silica Janus particles to the best of our knowledge.

To demonstrate the finite temperature difference across a Pt-silica Janus particle under laser illumination, we used fluorescence thermometry, in which the emission of a temperature-sensitive fluorescent dye, rhodamine B, was used to map the local temperature [62–65]. Isolated immobilized Janus particles (Fig 2(g inset)) and a partially coated monolayer of silica particles (EDF 2(d)) were exposed to a 532 nm defocused laser beam in a dilute rhodamine-B environment, which was excited by the same laser. A lower emission, *i.e.*, a darker appearance, indicates a higher local temperature in Pt-coated areas.

Optical trap setup – We used a linearly polarized 1064 nm TEM₀₀ mode Nd:YAG CW laser (Laser Quantum Opus 5 W) to set up an optical trap around a Nikon Eclipse Ti2-U inverted microscope [52]. The laser beam was first expanded and then tightly focused through an oil-immersion 60 \times 1.4 N.A. objective (Nikon CFI Plan APO Lambda), as shown in EDF 3(a). Spherically symmetric dielectric particles become harmonically confined at the point of focus [66].

Harmonic confinement for Janus colloids – The two hemispheres of the Pt-silica colloids have different optical properties at 1064 nm. While the uncoated side is almost transparent, the Pt-coated side reflects and absorbs most of the laser radiation with a transmittance of ~ 0.21 [57, 58]. In addition to conventional optical forces, scattering force (F_s) and gradient force (F_g), a thermophoretic force (F_t) that gives rise to thermophoretic propulsion, acts on the Janus

particle. These forces vary with both the instantaneous position and orientation of the particle, whereas the net force alters the orientational diffusion [8, 36, 39, 59, 67, 68]. The relative strengths and directions of these forces are shown for three typical position-orientations of a Janus particle in EDF 3(b).

We analyzed long-time position distribution of a thermophoretically active Pt-silica Janus particle in the optical trap at a lower laser power, $P = 4.14$ mW, where $\tau_R/\tau_k \ll 1$. The analytical prediction for the position distribution of an HBABP in this regime is Gaussian (Eq. 3) with the corresponding effective potential being quadratic (Eq. 5). Our experimentally observed position distribution and corresponding effective potential, obtained by Boltzmann inversion, fit well with Gaussian and quadratic function, respectively (Fig. 3(b)). This verifies that the time-averaged optical trap confinement is indeed harmonic for Janus particles. At $t \gg (\tau_R, \tau_k)$, as the Janus colloid experiences all possible orientations and positions in the trap, the instantaneous axis-asymmetric optical forces F_s and F_g are averaged to provide symmetric harmonic confinement. The force constant k of this harmonic confinement for a passive Pt-silica Janus colloid can be obtained from the measured k_{eff} (Fig. 3(b), EDF 7(c)) using Eq. 5.

Regulating of activity and confinement parameters – In the experimental realization, the activity and confinement parameters V , τ_R , and τ_k are coupled. Regulating the thermophoretic propulsion speed (V) by changing the laser power induces a proportional effect on the confinement strength, k , and consequently, an inverse effect on τ_k . We varied both the laser power (P) and H_2O_2 concentration (c) to regulate the relevant system parameters V and τ_R/τ_k independently. A lower P resulted in a weaker confinement (longer τ_k) and a lower thermophoretic propulsion speed (V), where c was varied to increase V with additional diffusiophoretic activity. In contrast, P was increased to enhance both the strength of confinement (shortened τ_k) and the thermophoretic activity (V).

Tracking particle position and orientation – Both free and optically trapped active dynamics were recorded at 500 Hz using an FLIR Grasshopper monochrome camera. After the initial processing of the frames, the Trackmate ImageJ plugin was used to track the particles and obtain $x(t)$, $y(t)$, and $\phi(t)$ [69]. While $x(t)$ and $y(t)$ were further analyzed to obtain the position distributions, velocity distributions, and MSDs, $\phi(t)$ provided an alternative way to determine τ_R .

Determining the parameters – We determined the relevant dynamical parameters, V and τ_R for free active motion and V , τ_R , and τ_k for active dynamics in the optical trap by fitting the experimental MSDs with Eq. 1 and Eq. 8 respectively. For a more reliable fitting over the entire range of MSDs of the free active dynamics, we used the weighted least squares (WLS) regression method [70]. For active motion in the optical trap, the estimated values of the parameters were first assessed by piecewise fitting the relevant regime of the MSDs, while image processing provided

a good estimation of τ_R . The estimated values of the parameters were then used for initialization to fit the full range of MSDs.

C | Langevin dynamics simulations of HBABP

Simulating HBABP trajectories – We numerically simulated Eq. 2 with the desired values of V , τ_R , and τ_k , where τ_R determined D_R and consequently D_T in water. The orientational Brownian displacement $\Delta\phi$ in time-step Δt was considered a normal random variable with mean zero and standard deviation $\sqrt{2D_R\Delta t}$. This provided the orientational time-series $\phi(t_i) = \phi(t_{i-1}) + \Delta\phi(\Delta t)$, where $t_i = t_{i-1} + \Delta t$. The translational dynamics were then simulated by adding propulsion components to the corresponding HBBP dynamics along both x and y at each time-step, as $x_{\text{HBABP}}(t_i) = x_{\text{HBBP}}(t_i) + V \cos(\phi(t_{i-1}))\Delta t$. The HBBP dynamics, *i.e.*, $x_{\text{HBBP}}(t_i)$ and $y_{\text{HBBP}}(t_i)$, with given D_T and τ_k , were conveniently obtained by employing Green's function:

$$G(x(t_i), x(t_{i-1}); \Delta t) = \frac{1}{[2\pi B(\Delta t)]^{1/2}} \exp\left(-\frac{(x(t_i) - A(\Delta t))^2}{2B(\Delta t)}\right)$$

which represents a Gaussian probability with time-dependent mean $A(\Delta t) = x(t_{i-1}) \exp(-\Delta t/\tau_k)$ and variance $B(\Delta t) = \frac{k_B T}{k} (1 - \exp(-2\Delta t/\tau_k))$ [49, 50].

Choosing an appropriate time-step size – Because of persistence in propulsion, choosing an appropriately short time-step is crucial in simulating ABP or HBABP dynamics. By simulating ABP trajectories with progressively shorter Δt and analytically calculating the rms value of the deviation in the active dynamics during Δt , we concluded that the deviation in the trajectory would become negligible ($\lesssim 0.5\%$) with further shortening of Δt beyond $\Delta t \approx 10^{-2} \times \tau_R$. Moreover, to capture the details of the equilibration dynamics of an ABP in the harmonic well, we used Δt that satisfied $\Delta t \lesssim (10^{-2} \times \tau_R, 10^{-2} \times \tau_k)$ in all our simulations.

Computing MSD from large trajectory data – We implemented a fast Fourier transform to speed up the computation of MSD from large time-series data ($\sim 10^8$ data points). The time-averaged MSDs (Fig. 5, EDF 6) were calculated as,

$$\begin{aligned} \langle \Delta x^2(\tau) \rangle_t &= \langle (x(t+\tau) - x(t))^2 \rangle_t \\ &= \langle x(t+\tau)^2 \rangle_t + \langle x(t)^2 \rangle_t - 2\langle x(t+\tau)x(t) \rangle_t. \end{aligned}$$

While the cross term was computed using a fast correlation algorithm, the square terms were converted into recursion relations to calculate the MSD efficiently.

D | Position and velocity distributions

Histogram plots of position distributions – For a better comparison of the normalized position distributions obtained from the experimentally captured (Fig. 3(d)) or simulated (Fig. 4(a, b), EDF 5(a)) trajectories, we kept the number of bins ($= 100$) the same for all histogram plots, where the bin sizes were determined by dividing the spread of the trajectory by 100.

Calculation and plotting of velocity distributions – While calculating the instantaneous residual velocity components, $v_{\text{res}}^r = \dot{r}$ and $v_{\text{res}}^\theta = r\dot{\theta}$, from the experimentally captured (Fig. 3(d)) and simulated (Fig. 4(a, b)) trajectories, we considered average values of $r(t)$ and $\theta(t)$ over 0.1 s to eliminate the high-frequency fluctuations. The averaging time-window was chosen to be 0.1 s as it is at least ten times shorter than the characteristic timescales (τ_R, τ_k), ensuring that v_{res} retains all the relevant and crucial dynamical information. In one experimental case ($P = 12.43$ mW), where $\tau_R < 1$ s, an appropriately short time window (0.04 s) was used for the averaging. All histogram plots of v_{res} distributions were generated using 100 bins with appropriate bin sizes to cover the range of v_{res} values (Fig. 3(e, f), 4(c, d), EDF 5(b)).

E | Comparison with HBBP dynamics

Root-mean-square value of v_{HBBP} – From the MSD expression of an HBBP in 1D [53], we can expand $\langle v(t)^2 \rangle$ as

$$\left\langle \left(\frac{x(t+\Delta t) - x(t)}{\Delta t} \right)^2 \right\rangle = \frac{2k_B T}{k\Delta t^2} \left(\frac{\Delta t}{\tau_k} - \frac{\Delta t^2}{2\tau_k^2} \right) = \frac{2D_T}{\Delta t} - \frac{D_T}{\tau_k}$$

for a small $\Delta t/\tau_k$, which is ≤ 0.1 in our case. Hence, the rms value of v_{HBBP} in 2D is given by $(v_{\text{HBBP}})_{\text{rms}} = \sqrt{(4D_T/\Delta t) - (2D_T/\tau_k)}$ (Fig. 6(a)).

Computation of PSD – The single-sided PSD of $x(t)$ and $y(t)$ are defined as $\text{PSD}_x = |X(f)|^2$ and $\text{PSD}_y = |Y(f)|^2$, where $X(f)$ and $Y(f)$ are the Fourier transforms of $x(t)$ and $y(t)$, respectively. We computed the PSDs from the simulated trajectories with $V = 10 \mu\text{m/s}$ (Fig. 6(c, e)) using the Welch method, which estimates the spread of the power of a signal across frequencies based on an improved periodogram spectrum estimation to reduce noise.

When $\tau_R > \tau_k$, the HBABP dynamics effectively reduces to that of HBBP along the radial direction at $r = V\tau_k$, with the harmonic confinement performing free azimuthal motion (Fig. 6(d)). In this case, only the highlighted thin slices of the green trajectory on the positive x - and y -axes were considered for the PSD computation to eliminate the effect of the azimuthal dynamics of harmonic confinement.

PSD in the absence of activity – In the absence of any activity ($V = 0$), the Langevin equation (Eq. 2) along x and y take the same form, representing HBBP dynamics,

$$\dot{x} + \frac{x}{\tau_k} = v_B^x = \frac{f(t)}{\gamma_T},$$

where $f(t)$ is the random Brownian force. Taking the Fourier transform and the square of both sides, we obtain

$$4\pi^2 (f^2 + f_0^2) |X(f)|^2 = \frac{1}{\gamma_T^2} |F\{f(t)\}|^2$$

where f is the frequency in the Fourier space and $f_0 = (2\pi\tau_k)^{-1}$. $|X(f)|^2$ and $|F\{f(t)\}|^2$ are the single-sided PSD of $x(t)$ and $f(t)$, respectively.

Conforming to FDT, the PSD of $f(t)$ is frequency-independent and is given by $4\gamma_T k_B T$. Therefore,

$$\text{PSD}_x = \text{PSD}_y = \frac{k_B T}{\pi^2 \gamma_T (f^2 + f_0^2)} = \frac{L_0^2}{f^2 + f_0^2},$$

which is a Lorentzian with corner-frequency f_0 (Fig. 6(e)) [52]. For a free Brownian particle, $f_0 = 0$; therefore, $\text{PSD}_x = \text{PSD}_y = D_T/\pi^2 f^2$ (Fig. 6(c, e)). An HBBP experiences free Brownian diffusion at $t \ll \tau_k$, i.e., at $f \gg f_0$, where the Lorentzian PSD_x and PSD_y exhibit the same $D_T/\pi^2 f^2$ variation (Fig 6(e)).

References –

- [1] S. Ramaswamy, The mechanics and statistics of active matter, *Annual Review of Condensed Matter Physics* **1**, 323 (2010).
- [2] P. Romanczuk, M. Bär, W. Ebeling, B. Lindner, and L. Schimansky-Geier, Active brownian particles: From individual to collective stochastic dynamics, *The European Physical Journal Special Topics* **202**, 1 (2012).
- [3] M. C. Marchetti, J. F. Joanny, S. Ramaswamy, T. B. Liverpool, J. Prost, M. Rao, and R. A. Simha, Hydrodynamics of soft active matter, *Reviews of Modern Physics* **85**, 1143 (2013).
- [4] M. E. Cates and J. Tailleur, Motility-induced phase separation, *Annual Review of Condensed Matter Physics* **6**, 219 (2015).
- [5] C. Bechinger, R. Di Leonardo, H. Löwen, C. Reichhardt, G. Volpe, and G. Volpe, Active Particles in Complex and Crowded Environments, *Reviews of Modern Physics* **88**, 045006 (2016).
- [6] E. Fodor and M. Cristina Marchetti, The statistical physics of active matter: From self-catalytic colloids to living cells, *Physica A: Statistical Mechanics and its Applications* **504**, 106 (2018).
- [7] J. R. Howse, R. A. L. Jones, A. J. Ryan, T. Gough, R. Vafabakhsh, and R. Golestanian, Self-Motile Colloidal Particles: From Directed Propulsion to Random Walk, *Physical Review Letters* **99**, 048102 (2007).
- [8] H.-R. Jiang, N. Yoshinaga, and M. Sano, Active Motion of a Janus Particle by Self-Thermophoresis in a Defocused Laser Beam, *Physical Review Letters* **105**, 268302 (2010).
- [9] G. Volpe, I. Buttinoni, D. Vogt, H.-J. Kümmerer, and C. Bechinger, Microswimmers in patterned environments, *Soft Matter* **7**, 8810 (2011).
- [10] U. Basu, S. N. Majumdar, A. Rosso, and G. Schehr, Active Brownian motion in two dimensions, *Physical Review E* **98**, 062121 (2018).
- [11] B. Ten Hagen, S. Van Teeffelen, and H. Löwen, Brownian motion of a self-propelled particle, *Journal of Physics: Condensed Matter* **23**, 194119 (2011).
- [12] M. Caraglio and T. Franosch, Analytic Solution of an Active Brownian Particle in a Harmonic Well, *Physical Review Letters* **129**, 158001 (2022).
- [13] U. Basu, S. N. Majumdar, A. Rosso, and G. Schehr, Long-time position distribution of an active Brownian particle in two dimensions, *Physical Review E* **100**, 062116 (2019).
- [14] A. P. Berke, L. Turner, H. C. Berg, and E. Lauga, Hydrodynamic attraction of swimming microorganisms by surfaces, *Physical Review Letters* **101**, 038102 (2008).
- [15] J. Elgeti and G. Gompper, Wall accumulation of self-propelled spheres, *EPL (Europhysics Letters)* **101**, 48003 (2013).
- [16] C. F. Lee, Active particles under confinement: Aggregation at the wall and gradient formation inside a channel, *New Journal of Physics* **15**, 055007 (2013).
- [17] T. Bäuerle, R. C. Löffler, and C. Bechinger, Formation of stable and responsive collective states in suspensions of active colloids, *Nature Communications* **11**, 2547 (2020).
- [18] F. A. Lavergne, H. Wendehenne, T. Bäuerle, and C. Bechinger, Group formation and cohesion of active particles with visual perception-dependent motility, *Science* **364**, 70 (2019).
- [19] M. Hennes, K. Wolff, and H. Stark, Self-Induced Polar Order of Active Brownian Particles in a Harmonic Trap, *Physical Review Letters* **112**, 238104 (2014).
- [20] A. P. Solon, M. E. Cates, and J. Tailleur, Active brownian particles and run-and-tumble particles: A comparative study, *The European Physical Journal Special Topics* **224**, 1231 (2015).
- [21] F. Ginot, I. Theurkauff, D. Levis, C. Ybert, L. Bocquet, L. Berthier, and C. Cottin-Bizonne, Nonequilibrium equation of state in suspensions of active colloids, *Physical Review X* **5**, 011004 (2015).
- [22] Y. Fily, A. Baskaran, and M. F. Hagan, Dynamics of self-propelled particles under strong confinement, *Soft Matter* **10**, 5609 (2014).
- [23] E. Ben-Isaac, E. Fodor, P. Visco, F. van Wijland, and N. S. Gov, Modeling the dynamics of a tracer particle in an elastic active gel, *Physical Review E* **92**, 012716 (2015).
- [24] H. Ribeiro and F. Potiguar, Lane formation and crystallization of active matter in a narrow channel, *Physica A: Statistical Mechanics and its Applications* **503**, 849 (2018).
- [25] N. Narinder, J. R. Gomez-Solano, and C. Bechinger, Active particles in geometrically confined viscoelastic fluids, *New Journal of Physics* **21**, 093058 (2019).
- [26] A. R. Sprenger, C. Bair, and H. Löwen, Active brownian motion with memory delay induced by a viscoelastic medium, *Physical Review E* **105**, 044610 (2022).
- [27] F. Moore, J. Russo, T. B. Liverpool, and C. P. Royall, Active brownian particles in random and porous environments, *The Journal of Chemical Physics* **158**, 104907 (2023).
- [28] A. Pototsky and H. Stark, Active Brownian particles in two-dimensional traps, *EPL (Europhysics Letters)* **98**, 50004 (2012).
- [29] D. Chaudhuri and A. Dhar, Active Brownian particle in harmonic trap: Exact computation of moments, and re-entrant transition, *Journal of Statistical Mechanics: Theory and Experiment* **2021**, 013207 (2021).
- [30] K. Malakar, A. Das, A. Kundu, K. V. Kumar, and A. Dhar, Steady state of an active Brownian particle in a two-dimensional harmonic trap, *Physical Review E* **101**, 022610 (2020).
- [31] I. Santra, U. Basu, and S. Sabhapandit, Direction reversing active brownian particle in a harmonic potential, *Soft Matter* **17**, 10108 (2021).
- [32] I. Buttinoni, L. Caprini, L. Alvarez, F. J. Schwarzendahl, and H. Löwen, Active colloids in harmonic optical potentials ^(a), *Europhysics Letters* **140**, 27001 (2022).
- [33] M. Baldovin, D. Guéry-Odelin, and E. Trizac, Control of active brownian particles: An exact solution, *Physical Review Letters* **131**, 118302 (2023).
- [34] S. C. Takatori, R. De Dier, J. Vermant, and J. F. Brady, Acoustic

- trapping of active matter, *Nature Communications* **7**, 10694 (2016).
- [35] F. Schmidt, H. Šípová-Jungová, M. Käll, A. Würger, and G. Volpe, Non-equilibrium properties of an active nanoparticle in a harmonic potential, *Nature Communications* **12**, 1902 (2021).
- [36] Y. Zong, J. Liu, R. Liu, H. Guo, M. Yang, Z. Li, and K. Chen, An Optically Driven Bistable Janus Rotor with Patterned Metal Coatings, *ACS Nano* **9**, 10844 (2015).
- [37] F. Schmidt, A. Magazzù, A. Callegari, L. Biancofiore, F. Cichos, and G. Volpe, Microscopic engine powered by critical demixing, *Physical Review Letters* **120**, 068004 (2018).
- [38] O. Dauchot and V. Démery, Dynamics of a Self-Propelled Particle in a Harmonic Trap, *Physical Review Letters* **122**, 068002 (2019).
- [39] D. Bronte Ciriza, A. Callegari, M. G. Donato, B. Çiçek, A. Magazzù, I. Kasianiuk, D. Kasyanyuk, F. Schmidt, A. Foti, P. G. Gucciardi, G. Volpe, M. Lanza, L. Biancofiore, and O. M. Maragò, Optically Driven Janus Microengine with Full Orbital Motion Control, *ACS Photonics* **10**, 3223 (2023).
- [40] G. Patil, E. Vashist, H. Kakoty, J. Behera, and A. Ghosh, Magnetic nanohelices swimming in an optical bowl, *Applied Physics Letters* **119**, 10.1063/5.0058848 (2021).
- [41] S. Das, G. Gompper, and R. G. Winkler, Confined active Brownian particles: Theoretical description of propulsion-induced accumulation, *New Journal of Physics* **20**, 015001 (2018).
- [42] F. Kümmel, B. ten Hagen, R. Wittkowski, I. Buttinoni, R. Eichhorn, G. Volpe, H. Löwen, and C. Bechinger, Circular motion of asymmetric self-propelling particles, *Physical Review Letters* **110**, 198302 (2013).
- [43] G. Szamel, Self-propelled particle in an external potential: Existence of an effective temperature, *Physical Review E* **90**, 012111 (2014).
- [44] E. Fodor, C. Nardini, M. E. Cates, J. Tailleur, P. Visco, and F. van Wijland, How far from equilibrium is active matter?, *Physical Review Letters* **117**, 038103 (2016).
- [45] L. Dabelow, S. Bo, and R. Eichhorn, How irreversible are steady-state trajectories of a trapped active particle?, *Journal of Statistical Mechanics: Theory and Experiment* **2021**, 033216 (2021).
- [46] W. Yan and J. F. Brady, The force on a boundary in active matter, *Journal of Fluid Mechanics* **785**, 785R1 (2015).
- [47] L. Caprini, H. Löwen, and U. Marini Bettolo Marconi, Chiral active matter in external potentials, *Soft Matter* **19**, 6234 (2023).
- [48] V. Nosenko, F. Luoni, A. Kaouk, M. Rubin-Zuzic, and H. Thomas, Active janus particles in a complex plasma, *Physical Review Research* **2**, 033226 (2020).
- [49] M. Khan and T. G. Mason, Trajectories of probe spheres in generalized linear viscoelastic complex fluids, *Soft Matter* **10**, 9073 (2014).
- [50] M. Khan and T. G. Mason, Random walks of colloidal probes in viscoelastic materials, *Physical Review E* **89**, 042309 (2014).
- [51] J. Liu and Z. Li, Controlled mechanical motions of microparticles in optical tweezers, *Micromachines* **9**, 232 (2018).
- [52] S. Halder, D. Chanda, D. Mondal, S. Kundu, and M. Khan, Optical micromanipulation of soft materials: Applications in devices and technologies, in *Soft Materials for Functional Applications* (Springer Nature Singapore, 2024) pp. 415–469.
- [53] M. Doi, *Soft Matter Physics* (Oxford university press, Oxford, 2013).
- [54] S. Chandrasekhar, Stochastic problems in physics and astronomy, *Reviews of Modern Physics* **15**, 1 (1943).
- [55] A. Perro, S. Reculusa, S. Ravaine, E. Bourgeat-Lami, and E. Duguet, Design and synthesis of Janus micro- and nanoparticles, *Journal of Materials Chemistry* **15**, 3745 (2005).
- [56] A. I. Campbell, S. J. Ebbens, P. Illien, and R. Golestanian, Experimental observation of flow fields around active Janus spheres, *Nature Communications* **10**, 3952 (2019).
- [57] W. S. M. Werner, K. Glantschnig, and C. Ambrosch-Draxl, Optical Constants and Inelastic Electron-Scattering Data for 17 Elemental Metals, *Journal of Physical and Chemical Reference Data* **38**, 1013 (2009).
- [58] G. Ghosh, Dispersion-equation coefficients for the refractive index and birefringence of calcite and quartz crystals, *Optics Communications* **163**, 95 (1999).
- [59] S. Nedev, S. Carretero-Palacios, P. Kühler, T. Lohmüller, A. S. Urban, L. J. E. Anderson, and J. Feldmann, An Optically Controlled Microscale Elevator Using Plasmonic Janus Particles, *ACS Photonics* **2**, 491 (2015).
- [60] H. Moyses, J. Palacci, S. Sacanna, and D. G. Grier, Trochoidal trajectories of self-propelled janus particles in a diverging laser beam, *Soft Matter* **12**, 6357 (2016).
- [61] D. Paul, R. Chand, and G. V. P. Kumar, Optothermal Evolution of Active Colloidal Matter in a Defocused Laser Trap, *ACS Photonics* **9**, 3440 (2022).
- [62] V. K. Natrajan and K. T. Christensen, Fluorescent Thermometry, in *Encyclopedia of Microfluidics and Nanofluidics*, edited by D. Li (Springer US, Boston, MA, 2008) pp. 750–759.
- [63] D. Ross, M. Gaitan, and L. E. Locascio, Temperature Measurement in Microfluidic Systems Using a Temperature-Dependent Fluorescent Dye, *Analytical Chemistry* **73**, 4117 (2001).
- [64] S. Duhr, S. Arduini, and D. Braun, Thermophoresis of DNA determined by microfluidic fluorescence, *The European Physical Journal E* **15**, 277 (2004).
- [65] J. Zhou, W. Yang, Y. Yin, S. Chen, B. Yan, J. Mu, and X. Qi, Non-linear temperature calibration equation for Rhodamine B in different solutions for wide-temperature-range applications, *Applied Optics* **58**, 1514 (2019).
- [66] A. Ashkin, J. M. Dziedzic, J. E. Bjorkholm, and S. Chu, Observation of a single-beam gradient force optical trap for dielectric particles, *Optics Letters* **11**, 288 (1986).
- [67] F. S. Merkt, A. Erbe, and P. Leiderer, Capped colloids as light-mills in optical traps, *New Journal of Physics* **8**, 216 (2006).
- [68] J. Liu, C. Zhang, Y. Zong, H. Guo, and Z.-Y. Li, Ray-optics model for optical force and torque on a spherical metal-coated janus microparticle, *Photonics Research* **3**, 265 (2015).
- [69] D. Ershov, M.-S. Phan, J. W. Pylvänäinen, S. U. Rigaud, L. Le Blanc, A. Charles-Orszag, J. R. W. Conway, R. F. Laine, N. H. Roy, D. Bonazzi, G. Duménil, G. Jacquemet, and J.-Y. Tinevez, TrackMate 7: Integrating state-of-the-art segmentation algorithms into tracking pipelines, *Nature Methods* **19**, 829 (2022).
- [70] M. R. Bailey, A. R. Sprenger, F. Grillo, H. Löwen, and L. Isa, Fitting an active Brownian particle's mean-squared displacement with improved parameter estimation, *Physical Review E* **106**, L052602 (2022).

Data availability – All data required to reach the conclusions of this study are presented in the article and its supplementary information files. Source data are provided with this paper

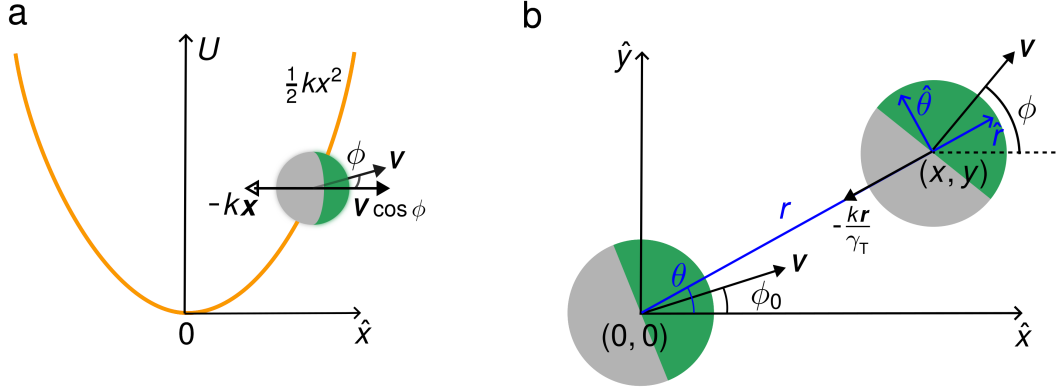
Code availability – The custom codes used in this work for numerical simulations are available from the corresponding author upon reasonable request.

Acknowledgments – The authors acknowledge the Science and Engineering Research Board (SERB), Govt. of India, for supporting this work through a Core Research Grant (CRG/2020/002723), and the PARAM Sanganak computing facility at the Computer Center, IIT Kanpur, for the numerical simulations. MK thanks Abhik Basu, Ambarish Ghosh, and Sriram Ramaswamy for fruitful discussions and critical reading of the manuscript.

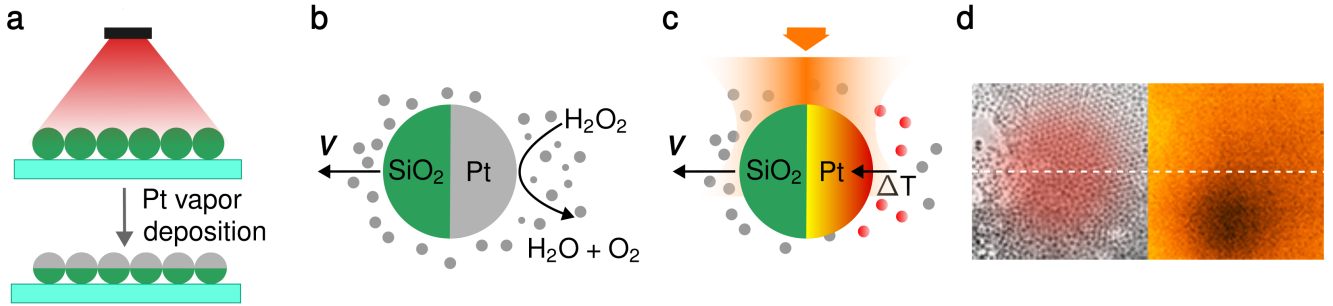
Author contributions – All the authors conceived and designed the research. SH performed analytical calculations, numerical simulations, and experiments, and analyzed the data. SH and MK interpreted data and wrote the manuscript. MK supervised the project.

Competing interests – The authors declare no competing interests.

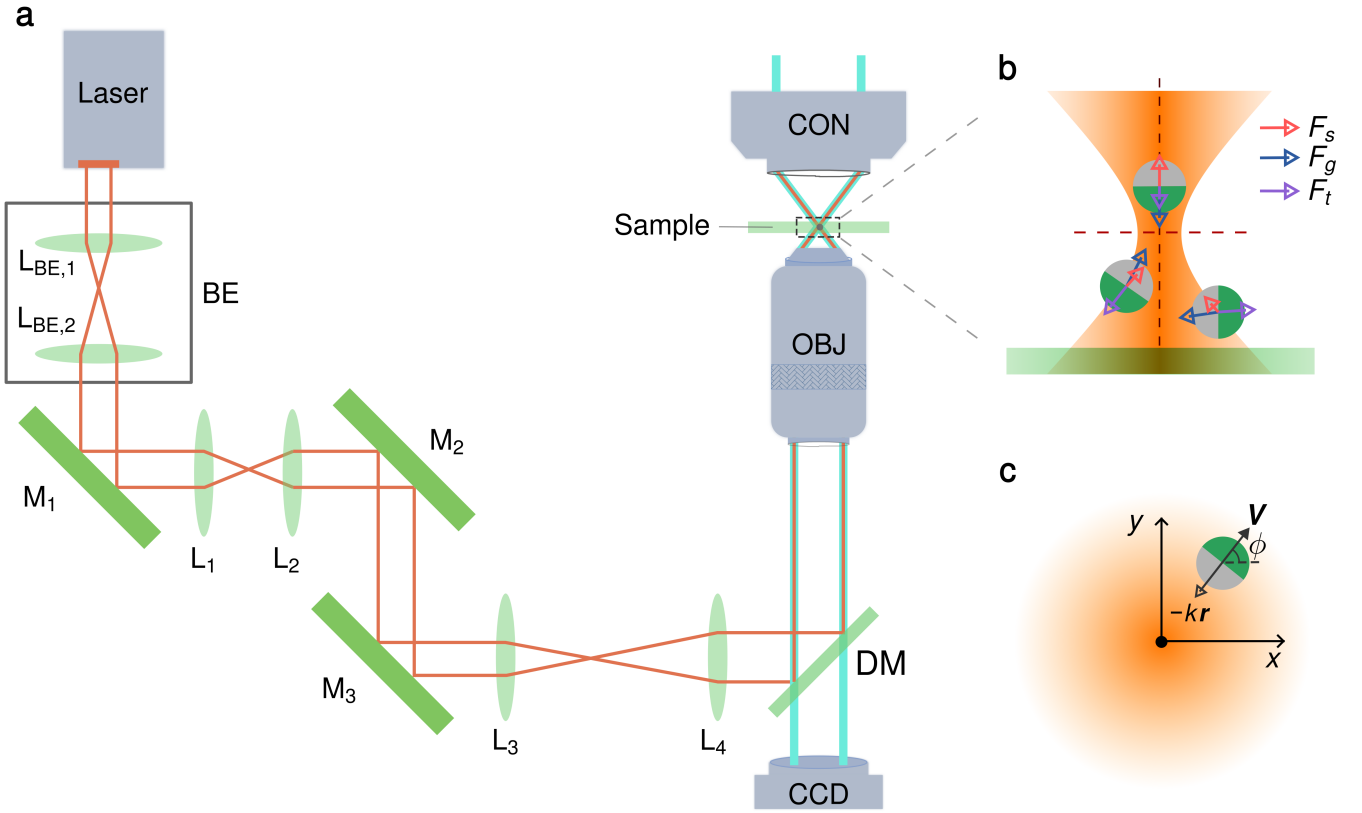
Extended data figures



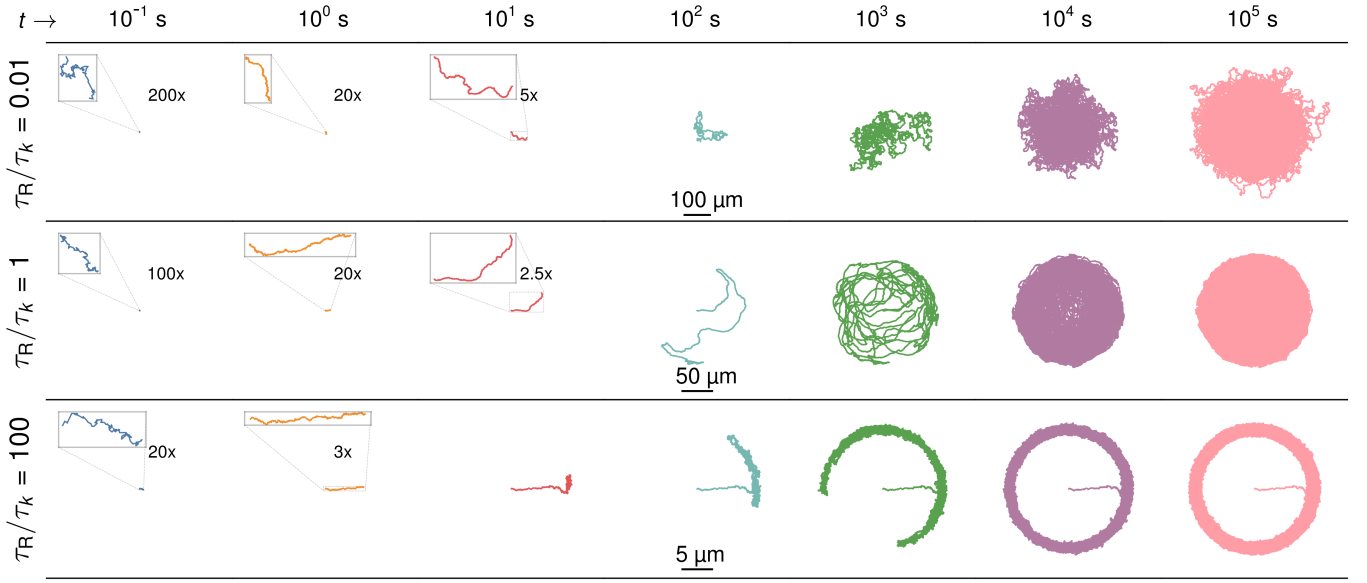
EXT. DATA FIG. 1. An active Brownian particle (ABP) in harmonic confinement. (a) Schematic shows an active Brownian particle, experimentally realized by a Pt-silica Janus colloid (grey-green), in a harmonic potential, given by $U = \frac{1}{2}kx^2$ (orange curve). The corresponding restoring force $(-kx)$ is pictorially represented by an open arrow. In addition, the Janus particle experiences active propulsion V , which has a constant speed and points from the Pt-coated side (gray) to the bare side (green), making an angle ϕ with the x -axis in the $x-y$ plane. The active velocity, V , and its x -component, $V \cos \phi$, are shown with solid arrows. (b) Active propulsion (V) and the restoring velocity $(-kr/\gamma_T)$ are shown in the $x-y$ plane for the initial ($t=0$) and typical position orientation at time t , with solid arrows. Starting from the origin $(0,0)$ with orientation ϕ_0 at $t=0$, the position and orientation of the Janus particles evolve to (x, y) and ϕ , respectively, at time t . In plane-polar coordinates (blue), the particle position is given by (r, θ) .



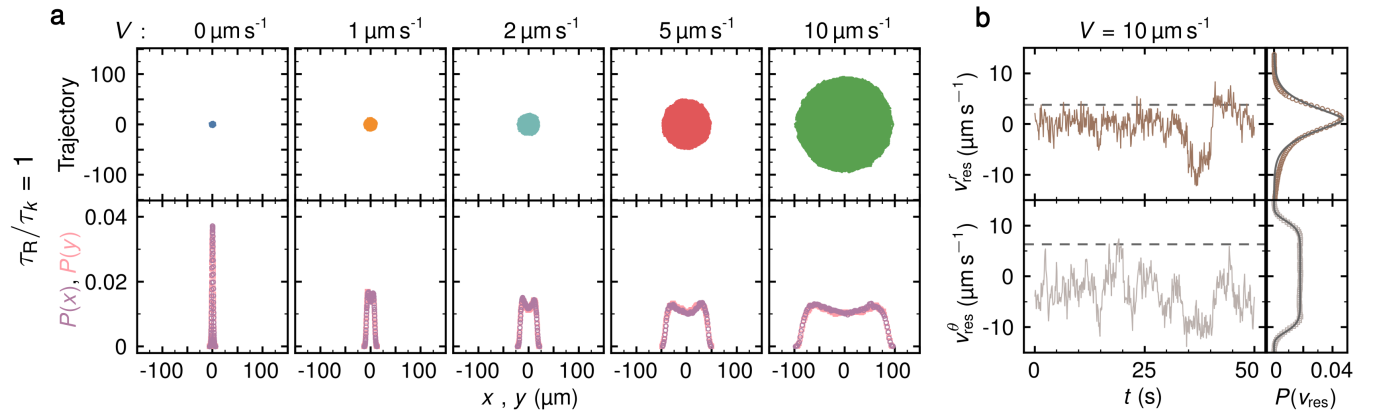
EXT. DATA FIG. 2. Phoretic active motion of Pt-silica Janus microspheres. (a) Platinum (Pt) vapor is deposited on a monolayer of silica microparticles (green circles) of diameter $1.76 \mu\text{m}$ by sputtering to obtain a Pt coating (grey) with a thickness of $\sim 5.5 \text{ nm}$ only on the top hemispheres (Fig. 2(a)). (b) When H_2O_2 is added to the suspension containing the Janus colloids, it dissociates into H_2O and O_2 at the Pt surface, which acts as a catalyst for the dissociation. The resultant concentration gradient causes diffusiophoretic active motion of the Janus particle with propulsion velocity V , which is directed towards the uncoated side (Fig. 2(b - d)). (c) The Pt-coated side becomes hotter than the bare side with a temperature gradient ΔT (red to yellow) when the Janus microsphere is exposed to laser radiation (orange). This temperature gradient induces thermophoretic active motion of the Janus particles. In this case too, the active motion with velocity V is directed along the uncoated side (Fig. 2(e - h)). (d) Fluorescence thermometry, under the exposure of a 532 nm defocused laser beam, demonstrates a higher local temperature at the Pt coating on the silica microspheres. Brightfield and fluorescence micrographs of a monolayer of silica microspheres, where the bottom part (marked by the white dashed line) is Pt-coated (appearing darker), are shown side by side. The defocused laser beam is shown as a red-gradient overlay on the bright-field image. The significantly lower emission of rhodamine B (orange) in the Pt-coated region indicates a higher local temperature. A similar fluorescent thermometry measurement on isolated single Pt-silica Janus particles is shown in the inset of Fig. 2(g).



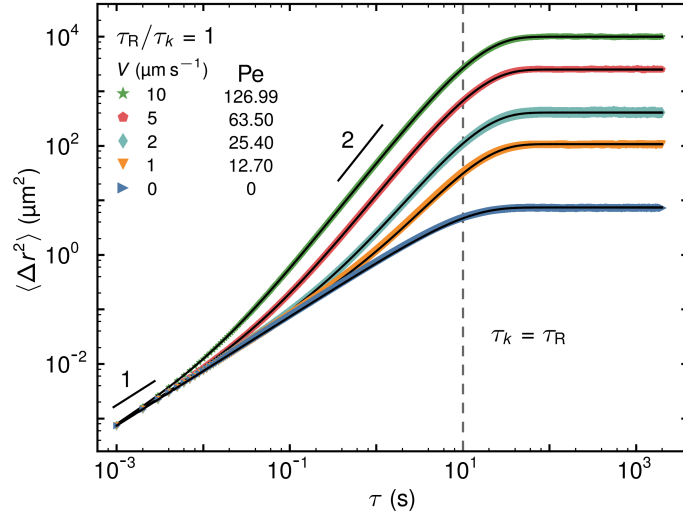
EXT. DATA FIG. 3. Optical trapping of Pt-silica Janus microparticles. (a) Schematic of an optical trap setup exhibits the beam path and optical components. An IR (wavelength: 1064 nm) laser beam is first expanded using a beam expander (BE) consisting of two lenses ($L_{BE,1}$ and $L_{BE,2}$) and sent to the objective (OBJ) through two afocal sets of lenses, (L_1, L_2) and (L_3, L_4), to achieve the desired expansion and steerability of the beam. M_1 , M_2 , and M_3 denote plane mirrors, and DM indicates a dichroic mirror that reflects the IR laser, allowing visible illumination light to pass through and fall on the CCD camera for imaging. The objective focuses the laser beam to a diffraction-limited spot to form an optical trap at the focal plane (Fig. 1(c), 3(a)), where the sample cell containing a suspension of the Pt-silica Janus colloids is placed. The condenser (CON) focuses the illumination on the sample for visualization and imaging. (b) A Pt-silica Janus microparticle (grey-green filled circle) experiences three forces in the laser field: scattering force (F_s), gradient force (F_g), and thermophoretic force (F_t), as indicated by red, blue, and violet open arrows, respectively (the same as those in Fig. 3(a)). The direction and magnitude of these forces vary with its instantaneous orientation and position in the optical field, as demonstrated for three typical situations. The beam axis is denoted by a dashed vertical line, and the horizontal dashed line indicates the focal plane. (c) The Janus microsphere is shown in the Gaussian intensity field of the laser (orange gradient) in the focal plane. While the restoring force $-kr$ is shown with an open arrow, the propulsion velocity V , making an angle ϕ with the x -axis, is indicated by a solid arrow.



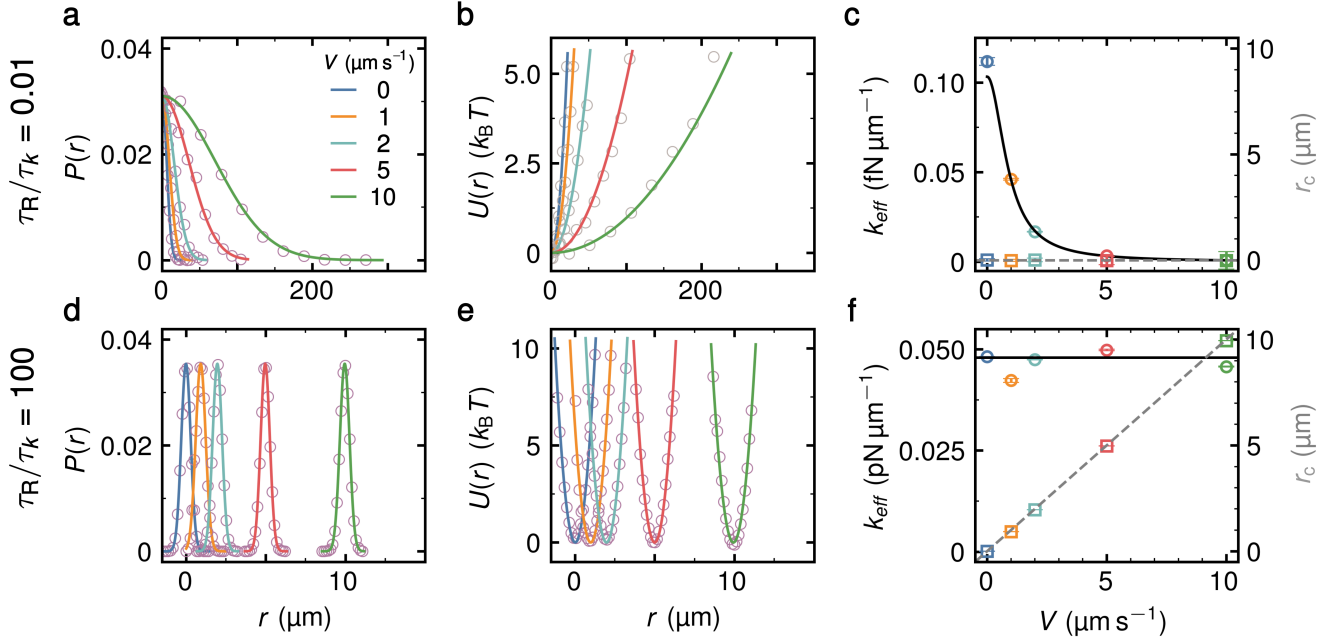
EXT. DATA FIG. 4. Time evolution of the simulated trajectories of an HBABP with propulsion speed $V = 10 \mu\text{m/s}$. The development of the 2D trajectories of the HBABP is shown for $\tau_R/\tau_k = 0.01, 1$, and 100 in three rows, from top to bottom, in seven steps, over a time span of seven decades starting from 10^{-1} s to 10^5 s as the system reaches a steady-state. For $\tau_R/\tau_k = 0.01$ with $\tau_R = 1$ s, and $\tau_k = 100$ s (top row), an isotropically progressing trajectory becomes bound and space-filling at a timescale ~ 100 s (Fig. 4(a) Supplementary Video 5). For $\tau_R = \tau_k = 10$ s (middle row), the trajectory becomes isotropic and bound at a time longer than 10 s, eventually filling a circular area with the lowest density at the center (EDF 5(a), Supplementary Video 7). At $\tau_R/\tau_k = 100$, with $\tau_R = 100$ s, and $\tau_k = 1$ s (bottom row), the trajectory grows along the initial propulsion direction and equilibrates at a radially displaced position. The equilibrated trajectory starts moving freely along the periphery of a circle, maintaining the same radial distance from the center of the harmonic well. The shape of the trajectory becomes apparent at a timescale of ~ 100 s, finally covering the full annular region at steady-state (Fig. 4(b) Supplementary Video 6). All trajectories in a row are shown at the same magnification, corresponding to the scale bar at the bottom center.



EXT. DATA FIG. 5. The simulated trajectories, position, and velocity distributions of an HBABP with $\tau_k = \tau_R$. (a) Steady-state (10^5 s) trajectories of an HBABP with $\tau_R = \tau_k = 10$ s are shown for increasing propulsion speed V from 0, essentially describing an HBBP, to $10 \mu\text{m/s}$ in blue, orange, cyan, red, and green in the top panel. The respective position distributions, $P(x)$ (purple circles) and $P(y)$ (pink squares), are displayed in the bottom panel. Interestingly, the trajectories are center-avoiding yet space-filling (Supplementary Video 7), as is evident from their bimodal position distributions in the steady-state. The spread of the trajectories, quantitatively described by the variance of the corresponding position distributions, increases with V . (b) A short span (50 s) of the time series and the probability distributions of the radial and azimuthal components of the residual velocity, v_{res}^r and v_{res}^θ , respectively, are shown for $V = 10 \mu\text{m/s}$. $P(v_{\text{res}})$ are fitted to super-Gaussian functions, $A \exp(-(|x - \mu|/w)^n)$, where w represents the width and n is the shape parameter. The probability distribution of v_{res}^r (open circles) fits well for $n = 1.44$ (peaked Gaussian, solid line), and that of v_{res}^θ (open squares) exhibits an excellent fitting for $n = 9.3$ (flat-top Gaussian, solid line). Comparatively smaller and higher rms values of v_{res}^r and v_{res}^θ , respectively, are marked with dashed horizontal lines in the time series plots. Thus, in this case, V^r is largely balanced by the restoring speed r/τ_k at a varied r (Eq. 7), whereas V^θ primarily contributes to the resulting dynamics.



EXT. DATA FIG. 6. MSDs from the simulated trajectories of an HBABP with $\tau_R = \tau_k = 10$ s. The computed MSDs from the simulated trajectories with five different propulsion speeds (V), starting from 0 (which exhibits HBBP dynamics) to $10 \mu\text{m/s}$ (EDF 5(a)), are shown with solid symbols of different colors. The colors and symbols of the MSDs corresponding to different V values and respective Péclet numbers (Pe) are given in the inset. The fittings of the MSDs to the analytical solution (Eq. 8) are shown with solid black lines. The dashed vertical line marks both τ_R and τ_k , which are equal. Apparent slopes of 1 and 2 are indicated by short black straight lines of the corresponding slopes as visual guides.



EXT. DATA FIG. 7. Variation in steady-state position distributions and corresponding effective harmonic confinements of HBABP with propulsion speed (V). The position distributions $P(r)$, effective quadratic potentials $U(r)$, their force constant k_{eff} , and radial position of the center r_c are shown for $V = 0$ (which corresponds to HBBP dynamics) to $10 \mu\text{m/s}$ in the two archetypal regimes (a – c) $\tau_R/\tau_k = 0.01$, and (d–f) $\tau_R/\tau_k = 100$. (a, d) The position distributions $P(r)$ obtained from the simulated trajectories at various V values (Fig 4(a, b)) are shown with open circles. They are fitted to Gaussians, following (a) Eq. 3 and (d) Eq. 4, which represent $P(x)$, but are equally applicable to $P(r)$ because of their circular symmetry, as represented by the solid lines of consistent colors (listed in the inset). (b, e) Effective confining potentials $U(r)$ are computed from the respective $P(r)$ by Boltzmann inversion and plotted with open circles, setting the reference to $U = 0$ at r_c . They fit well with quadratic functions $(1/2)k_{\text{eff}}(r - r_c)^2$, which are indicated by the color-coded solid lines. (c, f) Considering the position distributions in (a, b) as those of effective HBBPs, k_{eff} and r_c are obtained for varied V and plotted with color-coded open circles and squares, using the left and right vertical axes, respectively. These values of k_{eff} and r_c are equal to the corresponding values obtained from the quadratic fits of $U(r)$ (in b, e) within the fitting uncertainties. The variations in k_{eff} (black solid line) and r_c (grey dashed line) with V exhibit excellent agreement with (c) Eq. 5 and (f) Eq. 6. The error bars in k_{eff} and r_c correspond to uncertainties in the fitting parameters.